

Evolution of stress fields during crack growth and arrest in a brittle-ductile CrN-Cr clamped-cantilever analysed by X-ray nanodiffraction and modelling

M. Meindlhumer^{a,*}, L.R. Brandt^b, J. Zalesak^c, M. Rosenthal^d, H. Hruby^e, J. Kopecek^f, E. Salvati^{b,g}, C. Mitterer^h, R. Daniel^{a,h}, J. Todt^{c,h}, J. Keckes^h, A.M. Korsunsky^{b,i}

^a Christian Doppler Laboratory for Advanced Synthesis of Novel Multifunctional Coatings at the Department of Materials Science, Montanuniversität Leoben, Leoben, Austria

^b MBLEM - University of Oxford, Department of Engineering Science, Parks Road, Oxford OX1 3PJ, United Kingdom

^c Erich Schmid Institute for Materials Science, Austrian Academy of Sciences, Leoben, Austria

^d ESRF Grenoble, Grenoble, France

^e voestalpine eifeler Vacotec GmbH, Düsseldorf, Germany

^f Institute of Physics, Czech Academy of Science, Praha, Czech Republic

^g Polytechnic Department of Engineering and Architecture (DPIA), University of Udine, Via delle Scienze 208, Udine, 33100, Italy

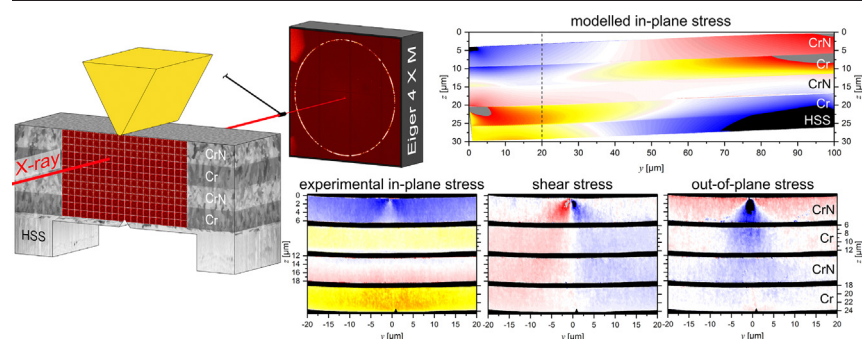
^h Department of Materials Science, Montanuniversität Leoben, Austria

ⁱ Diamond Light Source, Harwell Oxford, OX11 0DE, United Kingdom

HIGHLIGHTS

- Multi-axial residual stress distributions across a notched CrN-Cr clamped micro-cantilever were determined experimentally.
- Residual stresses in Cr introduce an effective stress intensity of $-5.9 \pm 0.4 \text{ MPa m}^{1/2}$, forming a plastic zone around the notch.
- Upon crack growth through Cr to the adjacent CrN-Cr interface, the crack is arrested there and its stress fields disappears.

GRAPHICAL ABSTRACT



ARTICLE INFO

Article history:

Received 24 August 2020

Received in revised form 2 November 2020

Accepted 25 November 2020

Available online 28 November 2020

Keywords:

Cross-sectional X-ray nanodiffraction

Micromechanics

CrN

Cr

Multi-layer

Eigenstrain modelling

ABSTRACT

In order to understand the fracture resistance of nanocrystalline thin films, it is necessary to assess nanoscopic multiaxial stress fields accompanying crack growth during irreversible deformation. Here, a clamped cantilever with dimensions of $200 \times 23.7 \times 40 \mu\text{m}^3$ was machined by focused ion beam milling from a thin film composed of four alternating CrN and Cr layers. The cantilever was loaded to 460 mN in two steps and multiaxial strain distributions were determined by *in situ* cross-sectional X-ray nanodiffraction. Characterization in as-deposited state revealed the depth variation of fibre texture and residual stress across the layers. The *in situ* experiment indicated a strong influence of the residual stresses on the cross-sectional stress fields evolution and crack arrest capability at the CrN-Cr interface. In detail, an effective negative stress intensity of $-5.9 \pm 0.4 \text{ MPa m}^{1/2}$ arose as a consequence of the residual stress state. Crack growth in the notched Cr layer occurred at a critical stress intensity of $2.8 \pm 0.5 \text{ MPa m}^{1/2}$. The results were complemented by two-dimensional numerical simulation to gain further insight into the elastic-plastic deformation evolution. The quantitative experimental and modelling

* Corresponding author.

E-mail address: michael.meindlhumer@unileoben.ac.at (M. Meindlhumer).

results elucidate the stepwise nature of fracture advancement across the alternating brittle and ductile layers and their interfaces.

© 2020 The Author(s). Published by Elsevier Ltd. This is an open access article under the CC BY-NC-ND license (<http://creativecommons.org/licenses/by-nc-nd/4.0/>).

1. Introduction

Mechanical integrity of thin films is determined not only by their extraordinary ultimate compressive and tensile strength, but also to a great extent by their ability to resist catastrophic failure due to instable crack propagation from pre-existing defects of various origins [1–3]. The discipline of linear elastic fracture mechanics (LEFM) was developed to quantify the ability of brittle materials to resist crack propagation [4,5]. Its underlying thermodynamic principle is to link the strain energy release rate due to crack growth with the energy required for the formation of new fracture surfaces. The elasticity solutions for the displacement, strain, and stress fields around the crack tip obtained within this framework contain singularities that violate the assumption of finite material deformability and strength. LEFM deals with this central contradiction by excluding from consideration the so-called process zone (PZ), where material decohesion occurs. Instead, attention is focused on the relevant parameters outside the PZ which are assumed to fully determine the conditions for crack propagation. Key parameters in this consideration are the stress intensity factors (SIF) K_I , K_{II} and K_{III} that define the severity of the equivalent conceptual elastic crack tip singularity. Hence, the annular zone surrounding the PZ is sometimes referred to as the K -zone. The sum of squared SIFs with elastic moduli as coefficients allows the strain energy release rate to be evaluated. LEFM is valid for brittle or semi-ductile materials, where plastic deformation is restricted to the relatively small plastic zone surrounding the process zone, itself embedded within the K -zone. It is important to note that even in these (semi-)brittle cases the stress singularity in front of a crack tip leads to plastic deformation and the formation of a plastic zone.

In mainly ductile materials the crack propagation is significantly affected by dislocation emission and plastic deformation, so that the size of the PZ is not small compared to the sample dimensions. Under these conditions of significant ductility, elastic-plastic fracture mechanics (EPFM) needs to be applied instead of LEFM. Hutchinson, Rice and Rosengren demonstrated in their model [6,7] that at stresses exceeding the yield strength of the elastic-plastic material, hardening controls the stress increase in front of the crack tip. The stress distribution within the plastic and process zones remains of high scientific interest, since the strains and stresses control the plastic deformation and material separation that ultimately leads to catastrophic failure. The experimental assessment of the strains/stresses within the confined volume of the plastic zone is of vital importance to understand the mechanisms of crack growth and failure.

According to the available literature, stress distributions in front of the crack tip have been investigated with neutron or synchrotron X-ray diffraction using gauge volumes of ~2 mm [8,9] and down to ~25 μm [10–15], respectively. Some of the reported experimental work has focused on (i) the influence of residual stresses on crack growth in compact tension (CT) samples fabricated from Al alloys, but most works were dedicated to resolving (ii) the influence of overload events on fatigue crack growth in standard sample geometries. In the former case, tensile residual stress in front of the crack tip led to a significant acceleration of (stable) crack growth during unidirectional loading of the sample [8,9]. However, standard fracture mechanics samples are not suitable for thin film testing due to their restricted thickness. In the field of micromechanical testing several cantilever-based geometries have therefore been proposed and developed [16,17]. In state-of-the-art experimental setup configurations, cantilevers can be tested *in situ* inside a scanning electron microscope (SEM) that allows following stable crack growth at the sample surface, and evaluating the fracture

toughness of the material on the basis of load–deflection and crack length-dependent stiffness data [17]. Digital Image Correlation (DIC) is usually a method of choice to map strain distributions at the sample surface. However, stress distributions within the material remain inaccessible to this technique without the use of additional assumptions (elastic relationship between strains and stresses), or further destructive testing steps [18]. Recent developments of the FIB-DIC technique have demonstrated its capability of mapping residual stresses at micron scale lateral resolution and better than 25 nm in the depth direction [19–21].

In prior studies CrN-Cr multilayer thin films have attracted significant interest because of their ability to withstand a broad range of mechanical loads without catastrophic failure, such as abrasive [24,25], indentation [26] and fracture mechanical loads [3,27]. As indicated by these studies, the introduction of Cr interlayers with varying thickness has a significant influence on the crack propagation behaviour and on the mechanical stability of CrN-Cr multilayer thin films. The ductile Cr interlayers and the CrN-Cr interfaces serve as crack deflection barriers and thus increase the resistance against catastrophic failure [3,24–27]. However, the stress acting at the crack tip and the influence of residual stress on crack propagation still remain unclear.

On the other hand, cross-sectional X-ray nanodiffraction (CSnanoXRD), described in detail in Refs. [21–23]) coupled with nano-indentation allows for *in situ* characterization of laterally and depth-dependent stress distributions generated in thin films with a spatial resolution down to $200 \times 200 \text{ nm}^2$, giving new insights into the deformation behaviour of exemplary nanoceramic monophasic TiN [22] and CrN [23], as well as the stress relief caused by cracking. These experiments revealed the key effect of abrupt changes of compressive residual stress parallel to the interfaces between individual layers of similar materials on the formation and growth of cracks. The nucleation of cracks in the top sublayer containing low residual stress is followed by crack re-orientation, extensive crack deflection and crack arrest phenomena observed at the interfaces of monophase sublayers [20] of different residual stresses.

The present study utilized *in situ* CSnanoXRD for the first time to investigate both the residual and loading-induced stresses during stepwise deformation of a CrN-Cr nano-multilayer clamped cantilever. The evolution of a plastic zone originating from a pre-milled notch and crack growth during mechanical loading were monitored, quantified, and correlated with established theoretical approaches. *In situ* experiments revealed the crack arrest effect of the interfaces between brittle CrN and ductile Cr layers, as well as crack tip blunting that could be seen at the highest applied load. The results were correlated with 2D numerical simulations using the eigenstrain-finite element method.

2. Experiment and methods

2.1. Thin film synthesis

For this study, a multi-layered CrN-Cr film consisting of four layers, each ~5 to 5.5 μm thick, was deposited on an electrolytically polished plate made of high speed steel (HSS) with lateral dimensions of $20 \times 20 \text{ mm}^2$ and a thickness of ~5 mm. The film was deposited by unbalanced magnetron sputtering using a powder-metallurgically produced Cr target. Prior to the deposition process, the chamber was evacuated to 10^{-4} Pa , the substrate was then heated to 350 °C and plasma etched for 10 min. The deposition was also performed at 350 °C and a total pressure of 1 Pa was applied. The Cr layers were deposited in a pure Ar atmosphere and an applied bias voltage of –40 V, whereas the CrN layers

were grown in an Ar + N₂ atmosphere applying a bias voltage of −80 V. The N₂ partial pressure was adjusted to 0.25 Pa using a capacitive gauge. The resulting overall thickness of the film was ~21.7 μm.

2.2. FIB-preparation and investigation of the cantilever

At first, a cross-sectional lamella for the CSnanoXRD experiment with a thickness of ~200 μm in beam direction was prepared from the thin film sample by mechanical polishing. In the next step, a Tescan FERA3 FIB using Xe⁺ ions at an acceleration voltage of 30 kV and a current of 300 nA was used to further cut the lamella down to a remaining thickness of 45 μm in a region with a length of 200 μm and to remove the substrate under the multilayer in this region. Prior to the cutting operations, a Si-mask was lifted-out using a micromanipulator, which was placed above the actual sample as a sacrificial protection to protect the sample surface from the high Xe⁺-ions currents. In order to cut the final geometry $L \times t \times B$ of the clamped cantilever to 200 μm × 23.7 μm × 40 μm, FIB machining was employed in a ZEISS Auriga CrossBeam Workstation by using Ga⁺ ions with a current of 13.6 nA. Finally, the notch was cut from the side on the bottom of the cantilever with a current of 500 pA. The cantilever was imaged prior to the experiment at an acceleration voltage of 5 kV and an aperture width of 60 μm using the SEM in-lens detector of the workstation. For post mortem imaging after the *in situ* CSnanoXRD experiment, a ~500 nm thick tungsten protection layer was deposited on the surface of the clamped cantilever using the gas injection system of the FIB workstation to protect the clamped cantilever surface from the Ga⁺ ion-damage. Afterwards, the cross-section was fine ion-polished at continuously reduced ion current from 5 nA to 500 pA and imaged with the secondary electron detector using a Ga⁺-ion current of 10 pA in order to reveal cross-sectional morphological features such as cracks, grain orientation variations and/or plastic deformation of the clamped cantilever resulting from the bending experiment.

2.3. CSnanoXRD experiment

The CSnanoXRD experiments was performed at beamline ID13 of the European Synchrotron (ESRF) in Grenoble, France [24] using the indenter setup developed for *in situ* indentation experiments and described in [23]. The nano-focussing lens (NFL) [25] setup was used to focus the X-ray beam with a photon energy of 14.9 keV to a spot of

150 nm in diameter and a focal depth of ~50 μm [24]. Prior to the CSnanoXRD experiment, at first the interfaces between the CrN and Cr layers were aligned parallel to the incident X-ray beam direction at two sample *z* positions by performing a set of absorption line-scans along the *z*-axis at various sample orientations around the *y*-axis (Fig. 1a) using a point X-ray detector [24,26]. The optimal sample orientation was determined by maximizing the X-ray absorption contrast between the CrN- and the Cr-layers. Subsequently, two-dimensional (2D) absorption scans (presented in Suppl. Fig. 1) were performed to locate the centre of the clamped cantilever and to determine the centres of the CSnanoXRD mesh scans. The clamped cantilever was incrementally loaded to 150 and 460 mN (cf. Fig. 1b), and four areas of 40 × 30 μm were characterized in detail by mesh scanning the sample along the *y*- and *z*- direction in 200 nm steps (i) before applying the load, (ii) at 150 mN load, (iii) at 460 mN load and (iv) after unloading. In total, 30,351 2D diffractograms were recorded for each step. The 2D diffraction signal was recorded by a Dectris Eiger X 4 M detector at each measurement position using an acquisition time of 50 ms. The exact detector geometry with respect to the sample was calibrated using a NIST LaB₆ powder, yielding a sample-to-detector distance of 152.60 mm. The evaluation of the 2D patterns containing CrN 111 and 200 or Cr 110 Debye-Scherrer rings (Fig. 1) was performed using the pyFAI software package [27,28].

2.4. CSnanoXRD data analysis

Qualitative texture analysis was carried out by a radial (θ) integration of the CrN 200 and Cr 110 Debye-Scherrer rings providing azimuthal intensity distributions $I^{m,hkl}(\delta, z)$ and the data were plotted as a function of the azimuthal angle δ , which is the angle between the film normal and the projection of the diffraction vector onto the detector (Fig. 1). The diffuse scattering at relatively small diffraction angles, i.e. small-angle X-ray scattering (SAXS), around the beam stop (Fig. 1) originates primarily from electron density variations, such as alternation of materials, presence of grain boundaries, interfaces, cracks, precipitates and pores with sizes of $\sim \lambda/\theta$, where λ represents the X-ray wavelength and θ is a half of the Bragg angle [29,30]. In the present case, the signal scattered onto the 2D detector at the diffraction angles of ~0.05 to ~0.5 degrees was integrated radially (θ) and azimuthally (δ) in order to obtain a qualitative information primarily on the occurrence of the growing crack within the clamped cantilever.

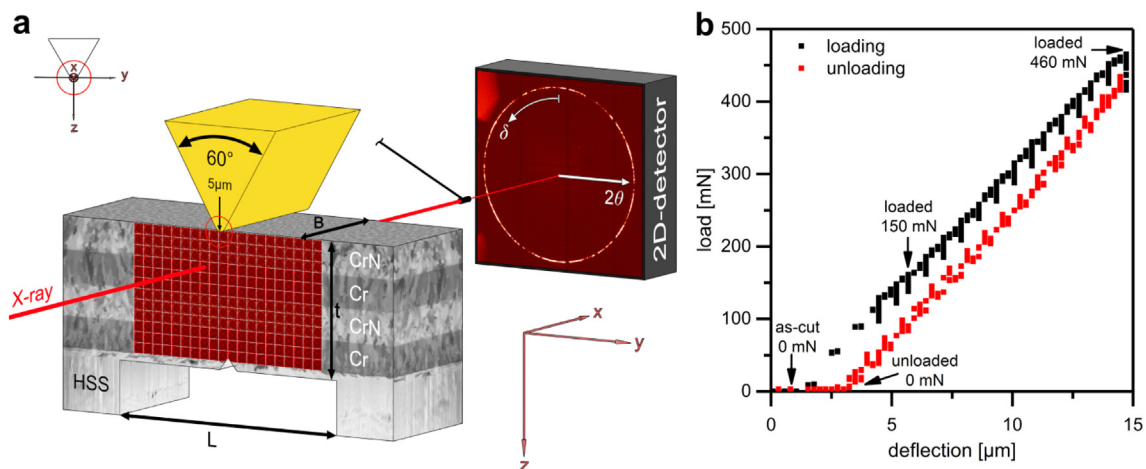


Fig. 1. (a) Schematic sketch of the *in situ* CSnanoXRD setup. A clamped cantilever cut from the sample lamella with dimensions of $L \times t \times B = 200 \times 23.7 \times 40 \mu\text{m}^3$, where L , B and t are the length, width and thickness of the clamped cantilever, respectively, was scanned with an X-ray beam of ~150 nm in diameter along *y* and *z* axes in steps of 200 nm. During the *in situ* CSnanoXRD experiment 30,351 2D diffraction patterns were recorded on an Eiger X 4 M CCD detector from $40 \times 30 \mu\text{m}^2$ large areas at each of the 4 load steps in the centre of the clamped cantilever. A detailed description of the *in situ* CSnanoXRD indentation setup is given in Ref. [23]. (b) Load-deflection curve of the clamped cantilever recorded during the *in situ* synchrotron experiment. The arrows indicate the load of 150 mN. 2D diffraction patterns for structural and stress analysis were recorded during the experiment (i) before loading (0 mN), (ii) at 150 mN, (iii) at 460 mN and (iv) after unloading (0 mN).

In order to evaluate the stress tensor distributions $\sigma_{ij}^m(y, z)$ with $i, j = x, y, z$, an integration of the diffraction patterns was performed over the azimuthal angle δ in $\Delta\delta$ segments of 10 deg. Thus, 36 radial intensity distributions $I(\theta, \Delta\delta)$ were obtained for each exposure. The positions of CrN 111 and 200 and Cr 110 diffraction peaks $\theta^{m, hkl}(\Delta\delta_g)$, $g = [1, 36]$ and, subsequently, the orientation-dependent lattice parameter $d_{\delta\theta}^{m, hkl}(y, z)$, were determined by fitting the X-ray diffraction patterns using a Pseudo-Voigt function in each cake g . The orientation-dependent lattice strain $\varepsilon_{\delta\theta}^{m, hkl}(y, z)$ for each phase m and corresponding Debye-Scherrer ring hkl was determined as follows

$$\varepsilon_{\delta\theta}^{m, hkl}(y, z) = \frac{d_{\delta\theta}^{m, hkl}(y, z) - d_0^{m, hkl}}{d_0^{m, hkl}} \quad (1)$$

where θ is the diffraction angle, δ the azimuthal orientation on the detector (cf. Fig. 1), $d_{\delta\theta}^{m, hkl}(y, z)$ is the lattice parameter obtained at the respective diffraction angle θ and azimuthal orientation δ and $d_0^{m, hkl} = a_0^m / (h^2 + k^2 + l^2)$ is the stress-free lattice spacing for a particular hkl reflection.

The unstressed lattice constant of CrN was determined from diffraction data near the surface of an undeformed region of the film, considering the stress-free out-of-plane orientation [31] and found to be $a_0^{\text{CrN}} = 0.41607$ nm. In the case of Cr, the stress-free lattice parameter $a_0^{\text{Cr}} = 0.28839$ nm was adopted from literature [32]. Since the Cr layers are never at a free surface, they are always exposed to inherent stress and hence no location with a stress-free orientation exists for this phase.

The measured orientation-dependent lattice strain $\varepsilon_{\delta\theta}^{m, hkl}(y, z)$ is a function of unknown dependent strain components $\varepsilon_{ij}^{m, hkl}$ with $i, j = x, y, z$ defined in the sample coordinate system as follows

$$\begin{aligned} \varepsilon_{\delta\theta}^{m, hkl}(y, z) = & \sin^2\theta \varepsilon_{xx}^{m, hkl}(y, z) + \cos^2\theta \sin^2\delta \varepsilon_{yy}^{m, hkl}(y, z) \\ & + \cos^2\theta \cos^2\delta \varepsilon_{zz}^{m, hkl}(y, z) - \sin 2\theta \cos\delta \varepsilon_{xz}^{m, hkl}(y, z) \\ & + \cos^2\theta \sin 2\delta \varepsilon_{yz}^{m, hkl}(y, z) - \sin 2\theta \sin\delta \varepsilon_{xy}^{m, hkl}(y, z) \end{aligned} \quad (2)$$

Using X-ray elastic constants $S_1^{m, hkl}$ and $\frac{1}{2}S_2^{m, hkl}$ the strain components $\varepsilon_{ij}^{m, hkl}$ of Eq. 2 can be replaced by the components of the stress tensor $\sigma_{ij}^m(y, z)$ defined in the sample coordinate system as follows

$$\begin{aligned} \varepsilon_{\delta\theta}^{m, hkl}(y, z) = & S_1^{m, hkl} [\sigma_{xx}^m(y, z) + \sigma_{yy}^m(y, z) + \sigma_{zz}^m(y, z)] \\ & + \frac{1}{2}S_2^{m, hkl} [\sin^2\theta \sigma_{xx}^m(y, z) + \cos^2\theta \sin^2\delta \sigma_{yy}^m(y, z) \\ & + \cos^2\theta \cos^2\delta \sigma_{zz}^m(y, z) - \sin 2\theta \cos\delta \sigma_{xz}^m(y, z) \\ & + \cos^2\theta \sin 2\delta \sigma_{yz}^m(y, z) - \sin 2\theta \sin\delta \sigma_{xy}^m(y, z)] \end{aligned} \quad (3)$$

X-ray elastic constants of $S_1^{\text{CrN}, 111} = -9.23 \times 10^{-7} \text{MPa}^{-1}$, $\frac{1}{2}S_2^{\text{CrN}, 111} = 4.446 \times 10^{-6} \text{MPa}^{-1}$, $S_1^{\text{CrN}, 200} = -2.99 \times 10^{-7} \text{MPa}^{-1}$, $\frac{1}{2}S_2^{\text{CrN}, 200} = 2.575 \times 10^{-6} \text{MPa}^{-1}$, $S_1^{\text{Cr}, 110} = 7.49 \times 10^{-7} \text{MPa}^{-1}$, $\frac{1}{2}S_2^{\text{Cr}, 110} = 4.441 \times 10^{-6} \text{MPa}^{-1}$ for CrN and Cr, respectively, were adopted from literature [33,34]. Concerning the evaluation of the as-deposited stress gradients within the thin film, the $\sin^2\psi$ -method can be adopted as follows

$$\begin{aligned} \varepsilon_{\delta\theta}^{m, hkl}(y, z) = & 2 S_1^{m, hkl} \sigma_{yy}^m(y, z) \\ & + \frac{1}{2} S_2^{m, hkl} \sigma_{yy}^m(y, z) [\sin^2\theta + \sin^2\delta \cos^2\theta] \end{aligned} \quad (4)$$

where the shear stresses along the planes parallel to the primary X-ray beam were neglected for simplicity and the in-plane stress state was estimated as equibiaxial $\sigma_{xx}^m(y, z) \approx \sigma_{yy}^m(y, z)$. Across the loaded cross-section of the clamped cantilever, the stress state was evaluated by least-squares fitting an overdetermined system of 36 linear equations

$$\begin{aligned} \varepsilon_{\delta\theta}^{m, hkl}(y, z) = & S_1^{m, hkl} [\sigma_{xx}^m(y, z) + \sigma_{yy}^m(y, z) + \sigma_{zz}^m(y, z)] \\ & + \frac{1}{2} S_2^{m, hkl} [\cos^2\theta \sin^2\delta \sigma_{yy}^m(y, z) + \cos^2\theta \cos^2\delta \sigma_{zz}^m(y, z) \\ & + \cos^2\theta \sin 2\delta \sigma_{yz}^m(y, z)] \end{aligned} \quad (5)$$

based on the measured lattice strain $\varepsilon_{\delta\theta}^{m, hkl}(y, z)$ evaluated for each cake g . It was assumed that the stress components $\sigma_{ij}^m(y, z)$ with $j = x, y, z$ did not change significantly during the cantilever loading due to the particular experiment geometry and therefore $\sigma_{xx}^m(y, z)$ values from the as-deposited state were considered in Eq. 5. whereby $\sigma_{xy}^m(y, z)$ and $\sigma_{xz}^m(y, z)$ values were neglected for simplicity.

2.5. 2D-simulation

In order to gain additional insight into stress and strain accommodation mechanisms within the CrN-Cr multilayer system before and during loading, a finite element (FE) model was created using the COMSOL Multiphysics® package. The cantilever dimensions were selected according to the SEM measurements shown in Fig. 2. The material properties employed are summarised in Table 1.

For all loading steps, the stress distribution within individual layers is a superposition of two main stress sources: (i) residual stress originating from processing, i.e. incident particles and thermal mismatch between coating and substrate σ_{res} (cf. Section 3.1.2) and (ii) bending/indentation stresses σ_{ext} arising from the external load applied by the indenter tip (F_{ind}). The residual stress σ_{res} at each point of the multilayer was modelled by prescribing the eigenstrain tensors $\varepsilon_{E, \text{Cr}}^*$ and $\varepsilon_{E, \text{CrN}}^*$ within the Cr and CrN layers, respectively. These tensors were obtained by iteratively solving the inverse problem of the eigenstrain reconstruction method (ERM) assuming that both the ductile behaviour of Cr interlayers as well as the more rigid behaviour of CrN layers contained either quadratic or constant eigenstrain distribution with respect to the film thickness direction. The eigenstrain component for Cr layers in horizontal direction $\varepsilon_{11, \text{Cr}}^*$ was assumed to follow a quadratic function distribution. In contrast, the vertical component $\varepsilon_{33, \text{Cr}}^*$ and the out-of-plane component $\varepsilon_{22, \text{Cr}}^*$ were modelled as constant. For the CrN layers, all eigenstrain components were chosen to be constant. These assumptions and resulting eigenstrain distributions were validated by comparing the residual stress resulting from the FE modelling with the experimental data from Fig. 3c. As a result, the following eigenstrain tensors were used for the simulation:

$$\varepsilon_{E, \text{Cr}}^* = \begin{pmatrix} a\varepsilon_{11, \text{Cr}}^{*2} + b\varepsilon_{11, \text{Cr}}^* + c & 0 & 0 \\ 0 & \varepsilon_{22, \text{Cr}}^* & 0 \\ 0 & 0 & \varepsilon_{33, \text{Cr}}^* \end{pmatrix} \quad (6)$$

$$\varepsilon_{E, \text{CrN}}^* = \begin{pmatrix} \varepsilon_{11, \text{CrN}}^* & 0 & 0 \\ 0 & \varepsilon_{22, \text{CrN}}^* & 0 \\ 0 & 0 & \varepsilon_{33, \text{CrN}}^* \end{pmatrix} \quad (7)$$

For the pre-loaded reference state, a small notch through the HSS substrate was added to the model of the clamped cantilever, as shown in Fig. 4. Finally, linear elastic material properties and symmetry along the vertical centreline of the cantilever were assumed. Subsequently, the indentation loads $F_{\text{ind}} = 150$ and 460 mN were applied at the centre of the clamped cantilever, keeping the found eigenstrain distribution unchanged to ensure that the residual stress was accounted for during the simulation of the indentation. As the experimental SAXS map data (cf. Fig. 4) clearly indicates the formation of a crack through the Cr layer opposite of the indenter tip after the initial loading, the same crack was considered in the FE model at 460 mN to account for this effect. The simulation results will be discussed in Section 3.3.

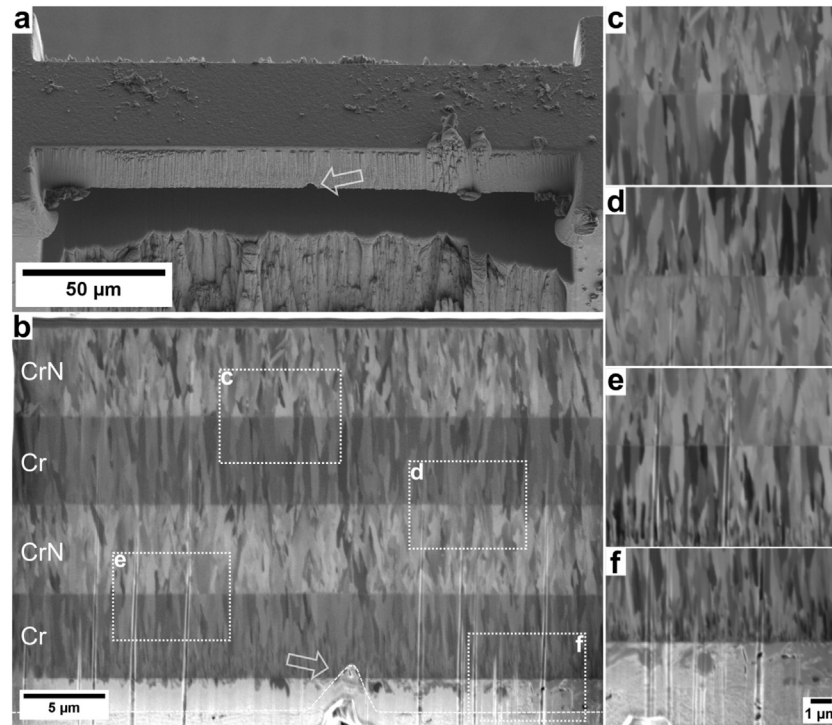


Fig. 2. (a) SEM micrograph of the as-fabricated clamped cantilever at an inclination of 45 deg. and (b) its cross-section prepared after the *in situ* CSnanoXRD synchrotron experiment. SEM cross-sectional micrographs showing in detail individual interfaces marked with the dashed rectangles in (b) from top to bottom between (c) CrN and Cr, (d) Cr and CrN, (e) CrN and Cr and (f) Cr and HSS substrate. The arrows indicate the position of the notch.

3. Results

3.1. Ex situ thin film analysis

3.1.1. Ex situ microstructural investigations

The as-fabricated clamped cantilever is shown in Fig. 2a at an inclination of 45 deg. The length and width of the cantilever were ~ 200 and $40 \mu\text{m}$, respectively. The cross-section of the clamped cantilever prepared by FIB at the centre of the sample after the *in situ* CSnanoXRD experiment revealed a dense, columnar-grained microstructure in all 4 layers of the film (Fig. 2b). The SEM inspection of the sample revealed a remaining portion of the substrate with a thickness of $\sim 2 \mu\text{m}$ (Fig. 2b), which was not fully removed by FIB. The notch milled by FIB with a total depth of $\sim 2.7 \mu\text{m}$ thus resulted in a notch in the Cr sublayer with a depth of $\sim 700 \text{ nm}$. The total thickness of the cantilever was $\sim 23.7 \mu\text{m}$. The thickness of individual Cr and CrN layers ranged between 5.2 and $5.5 \mu\text{m}$. Furthermore, a quasi-epitaxial relationship between CrN and Cr was revealed by a constant channelling contrast of the individual Cr and CrN grains across the CrN-Cr interface in the FIB-image (Figs. 2c–e), along with the absence of fine-grained nucleation layers, as observed also elsewhere [32]. No such structural relation was found for the Cr sublayer grown on the HSS substrate (Fig. 2f). Although a relatively coarse-grained microstructure of the CrN layers would be expected throughout the multilayer [32], the CrN layers were rather fine-grained with grain size in the range of 300 ± 30 and $830 \pm 150 \text{ nm}$

parallel and perpendicular to the interfaces, respectively, which is related to the intense ion bombardment assisting the layer growth. This is in contrast to the coarse-grained Cr layers grown at moderate bias voltage (Fig. 2b) [32,36].

3.1.2. Ex situ CSnanoXRD analysis

Results of the CSnanoXRD analysis performed *ex situ* on an undeformed region of the sample are shown in Fig. 3. Fig. 3a shows averaged diffraction data including Cr 110, CrN 111 and 200 reflections and reflections emanating from the substrate. In addition, weak Cr_2N reflections were detected in the transition zones in the vicinity of the CrN-Cr interfaces (Fig. 3a). The sharp transition between the individual Cr and CrN sample regions confirms the excellent sample alignment with respect to the incident X-ray beam, also documented by Suppl. Fig. 1.

Diffraction data from the non-deformed region were furthermore used for qualitative texture analysis. In the lower Cr sublayer, a $\langle 102 \rangle$ fibre texture was detected across the whole layer thickness, as evident by the azimuthal maxima of the 110 Debye-Scherrer ring at azimuthal angles of ± 15 , ± 45 and $\pm 75 \text{ deg.}$ in Fig. 3b. The following CrN sublayer is characterized by a $\langle 311 \rangle$ fibre texture near the CrN-Cr interface, which gradually changes into a $\langle 111 \rangle$ fibre texture. This texture cross-over is evident by a change of the position of the azimuthal maxima of the 200 Debye-Scherrer ring from ± 25 and $\pm 72 \text{ deg.}$ to $\sim \pm 55 \text{ deg.}$ The pronounced $\langle 110 \rangle$ texture of the top Cr layer completely differs to that of the Cr layer grown on the substrate surface. While the growth of the Cr layer on the HSS substrate is controlled only by fundamental growth mechanisms associated with the minimization of the strain energy at the initial growth stages and kinetic restrictions at greater layer thicknesses resulting in the $\langle 102 \rangle$ texture, the growth of the 110-oriented Cr grains on the top of the CrN layer with $\langle 111 \rangle$ texture was stimulated by the mutual epitaxial relationship between Cr and CrN grains. It can be expressed as $\{111\}_{\text{CrN}} \parallel \{110\}_{\text{Cr}}$. Epitaxial alignment of the top CrN sublayer along the 110-oriented Cr grains resulted in a subsequent development of the $\langle 311 \rangle$ fibre texture of the topmost CrN layer. The gradual

Table 1

Material properties of Cr and CrN layers and HSS substrate employed for the FE simulation.

Material	Young's modulus E [GPa]	Poisson's ratio ν
Cr [32]	279	0.21
CrN [35]	220	0.20
HSS	210	0.29

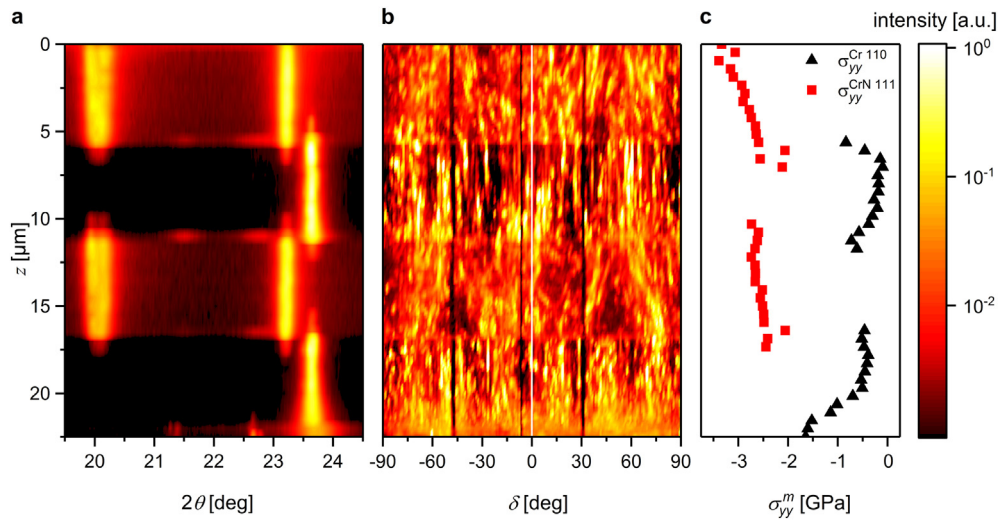


Fig. 3. Phase plot displaying azimuthally averaged intensities of CrN 111 and 200, as well as Cr 110 Debye-Scherrer rings (a), the azimuthal intensity distributions of CrN 200 and Cr 110 Debye-Scherrer rings (b) and in-plane distribution of average residual stress $\sigma_{yy}^m(z)$ in individual CrN and Cr layers (c). $z = 0 \mu\text{m}$ corresponds to the film surface, $z = 22.5 \mu\text{m}$ corresponds to the film/substrate interface.

texture cross-over from a rather weak $\langle 311 \rangle$ fibre texture into a strong $\langle 111 \rangle$ fibre texture was driven by the kinetic restrictions associated with a high bias voltage assisting growth of the CrN layer. Moreover, the alignment of $\langle 311 \rangle_{\text{CrN}}$ grains of the lower CrN layer on $\langle 102 \rangle_{\text{Cr}}$ grains of the lower Cr layer is consistent with the epitaxial relationship $\{100\}_{\text{CrN}} \parallel \{100\}_{\text{Cr}}$, reflected by the intensity maxima at ± 25.3 and ± 26.6 deg. off the out-of-plane axis, respectively, which is commonly observed and extensively discussed in literature [32,37,38].

Fig. 3c shows the as-deposited stress state across the undeformed film. Compressive stress in Cr layers ranges between -0.15 and ~ -1.60 GPa and between -2.45 and -3.40 GPa in CrN layers.

The compressive stress state in all layers is a result of (i) a dominant high-energy ion bombardment-assisted growth of the film and (ii) compressive stress build-up associated with the mismatch of the coefficients of thermal expansion between the layers and substrate ($\alpha_{\text{HSS}} > \alpha_{\text{Cr}} > \alpha_{\text{CrN}}$) and the subsequent development of compressive thermal stress during cooling of the coated sample from the deposition temperature down to room temperature. The variation of the compressive stress between individual layers is given by different energetic growth conditions (Cr layers were deposited at lower bias voltages than the CrN layers), the variation of the stress state within individual layers, however, has a different origin. It is predominantly given by

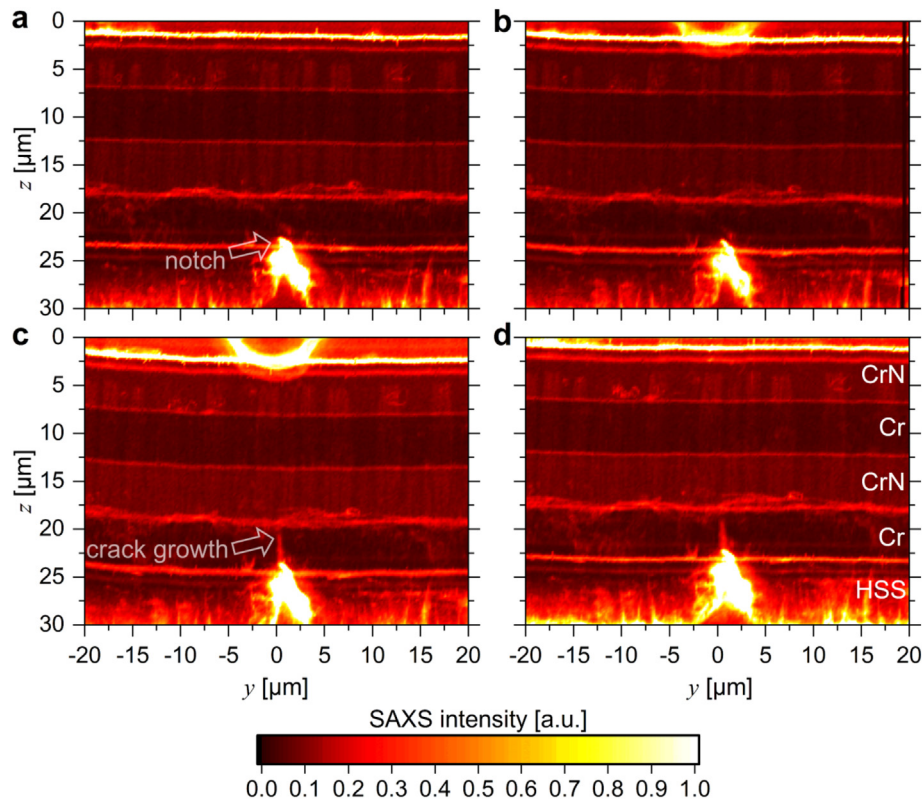


Fig. 4. SAXSM micrographs of the clamped cantilever (a) in the as-fabricated state, (b) during loading at 150 mN, (c) at a 460 mN load and (d) after unloading.

the variation of the crystallite size and associated defect density gradients within individual layers [32,38,39]. Much higher compressive stress up to -1.6 GPa was thus observed in the nucleation layer of the lower Cr sublayer (cf. Fig. 3c), which decreases to ~ -0.5 GPa as the Cr grains increase in size (cf. Fig. 2b). On the other hand, the stress state in the top Cr layer varies to much a lower extent (from -0.7 to -0.15 GPa), due to fairly constant Cr grain size throughout the layer, promoted by the local epitaxial growth of Cr on the fine-grained CrN sublayer [26]. In both CrN layers, residual stress gradually increases over the film thickness, which is associated with multiple re-nucleation events during growth, resulting in repeated reduction of the grain size and increased contribution of the compressive intrinsic stress to the overall stress state (Figs. 3c). Although the ion bombardment conditions did not change between the two CrN layers, the stress gradient in the top CrN sublayer is more pronounced compared to the lower CrN layer. This can be attributed to microstructural effects, such as crystallite realignment, deformation and splitting, originating from incoming accelerated particles from the plasma discharge [2,15]. Residual stress gradients emerging from deposition of thin films (Fig. 3c) have been investigated thoroughly in our earlier reports [32,39] and are out of the scope of this work.

3.2. In situ experiment

3.2.1. Load-displacement data

Fig. 1b shows the load-displacement curve recorded during the *in situ* CSnanoXRD experiment. During loading to ~ 450 mN, only a linear-elastic response was observed, while plastic deformation is not visible. The periodic load drops are related to the stepwise movement of the piezo actuator that is used to load the sample. At loads higher than 450 mN, the change in the slope of the curve indicates a change in stiffness of the cantilever, which is attributed to formation and

growth of cracks (Fig. 1b). The unloading is fully elastic without indications of inelastic changes in the material.

3.2.2. Small-angle X-ray scattering microscopy

Fig. 4 presents small-angle X-ray scattering microscopy (SAXSMs) micrographs compiled from the integrated intensities close to the direct beam, collected at 4 selected load steps (cf. Section 2.3) during the *in situ* experiment (before loading, at 150 and 460 mN and after unloading). In the as-fabricated state, the individual Cr and CrN layers can be clearly distinguished due to their different scattering intensity (Fig. 4a). Furthermore, the CrN-Cr interfaces, the remaining part of the substrate with a thickness of ~ 2 – 4.5 μm and the notch, penetrating ~ 700 nm into the first Cr layer, are clearly visible. At a load of 150 mN, bending of the cantilever was initiated by the indenter, as indicated by translation of the CrN-Cr interfaces from their original positions (Fig. 4b). An excellent lateral alignment of the indenter and notch indicates symmetrical loading conditions, with a lateral misalignment between indenter tip and notch of only $f \approx 0.8$ μm , which allows for a precise data interpretation. This alignment is critical for the experiment, because the ratio between mode II stress intensity K_{II} (in-plane shear mode) and mode I stress intensity K_I (crack-opening mode) is proportional to the misalignment between the indenter tip and notch over the length of the beam $\frac{f}{L}$ and inversely proportional to the aspect ratio of the cantilever $\frac{f}{L}$ [40,41].

Consequently, during evaluation of stresses and stress intensities applied to the clamped cantilever, K_{II} can be neglected [40]. The SAXS micrograph recorded at the maximum load of 460 mN (Fig. 4c) reveals the formation of a crack at the tip of the notch, which is responsible for the change of the slope of the load-displacement curve in Fig. 1b. After the release of the indenter tip, the interfaces realigned, leaving only slight residual curvature in the region located directly underneath the contact area with the indenter tip (Fig. 4d).

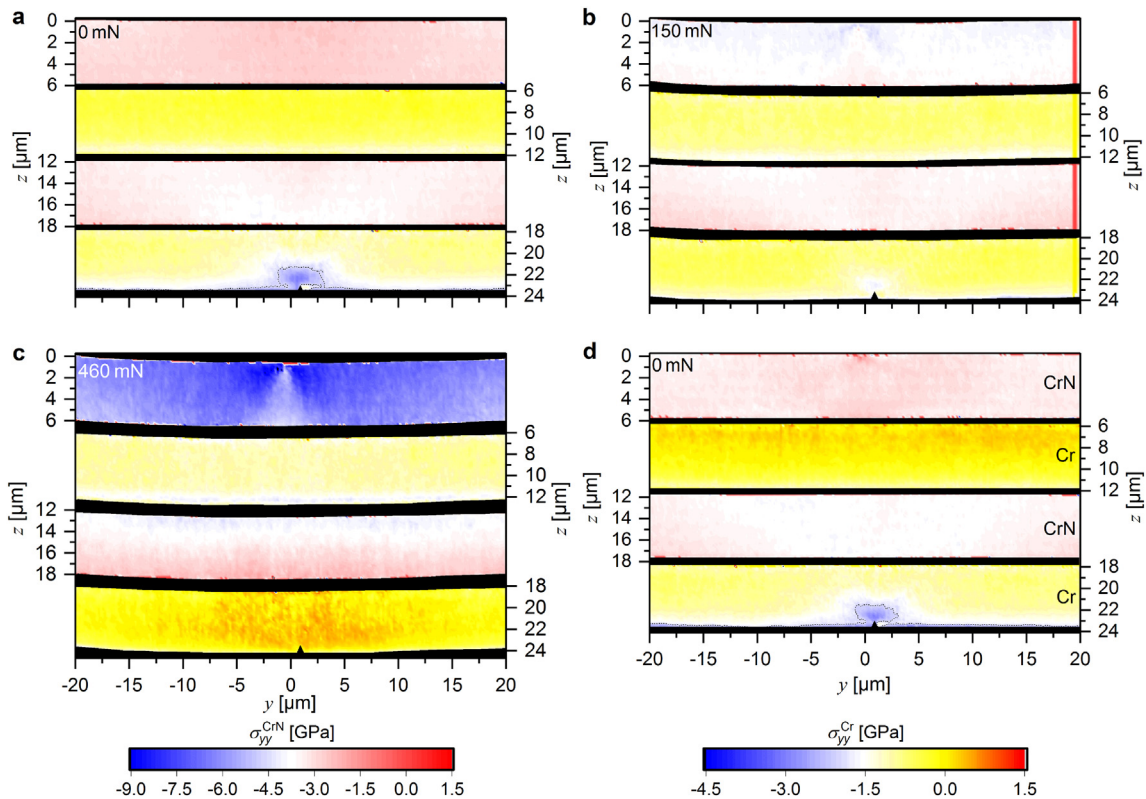


Fig. 5. In-plane/horizontal stresses $\sigma_{yy}^m(y,z)$ in the CrN and Cr layers of the clamped cantilever (a) in the as-fabricated state, (b) during loading at 150 mN, (c) at a 460 mN load and (d) after unloading. The isostress-line in (a) and (d) at -2 GPa shows the different stress concentrations in front of the initial notch before and after loading, respectively. The data at each individual load step were evaluated from 30,351 2D diffraction patterns. Note the different stress levels in the colour code for CrN and Cr.

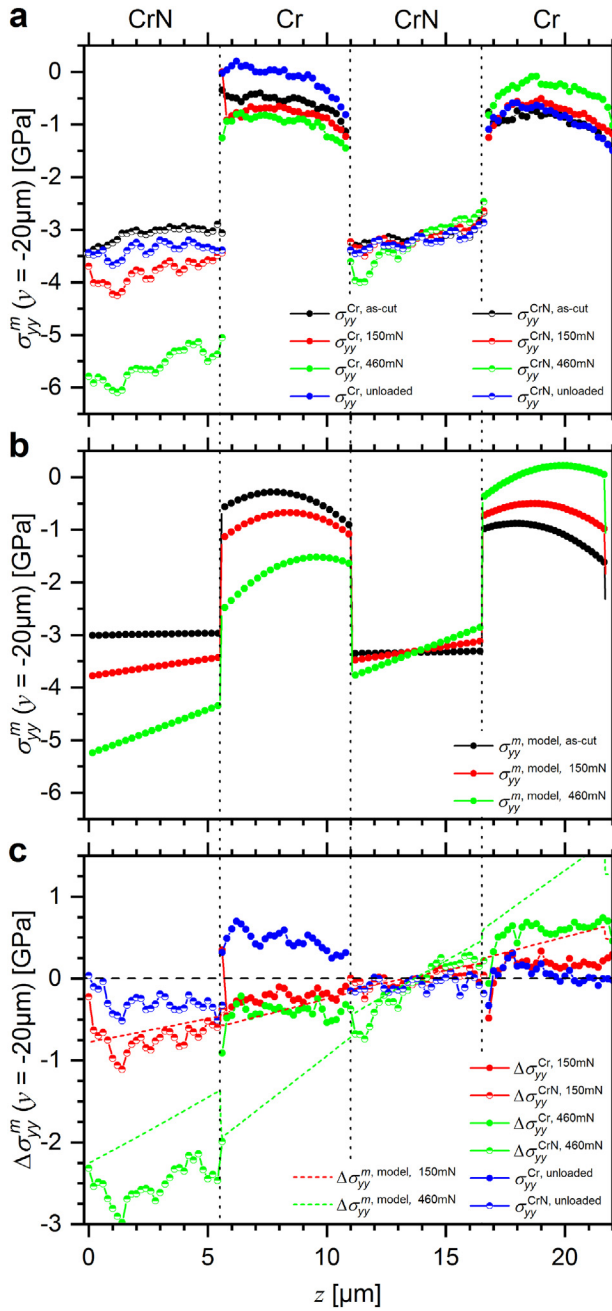


Fig. 6. In-plane/axial stress magnitudes $\sigma_{yy}^m(z)$ far off the notch ($y = -20 \mu\text{m}$) for (a) CrN and Cr inside the clamped cantilever at selected loads during the *in situ* experiment, (b) in-plane/axial stress magnitudes σ_{yy} far off the notch ($y = -20 \mu\text{m}$) for CrN and Cr of the clamped cantilever calculated using the ERM, and (c) the difference between the stress at the selected loads and the residual stress in as-fabricated state $\Delta\sigma_{yy}^m = \sigma_{yy,i} - \sigma_{yy,\text{as-cut}}$ for the experiment and simulation. The dashed vertical lines show the interfaces between Cr and CrN. $z = 0 \mu\text{m}$ corresponds to the indented film surface, $z = 22.5 \mu\text{m}$ corresponds to the film/substrate interface and the position of the notch.

3.2.3. Experimental stress results

The stresses evaluated from the *in situ* experiment according to Section 2.4 are presented here, in the context of linear-elastic (LEFM) and elastic-plastic (EPFM) fracture mechanics.

3.2.3.1. Experimental in-plane stresses. The in-plane stress distributions $\sigma_{yy}^m(y, z)$ at different stages of the *in situ* experiment on the CrN-Cr clamped cantilever are presented over the entire measurement area in Fig. 5 and in the form of a vertical section at position $y = -20 \mu\text{m}$ in Fig. 6. The stress state in the as-fabricated cantilever far away from the

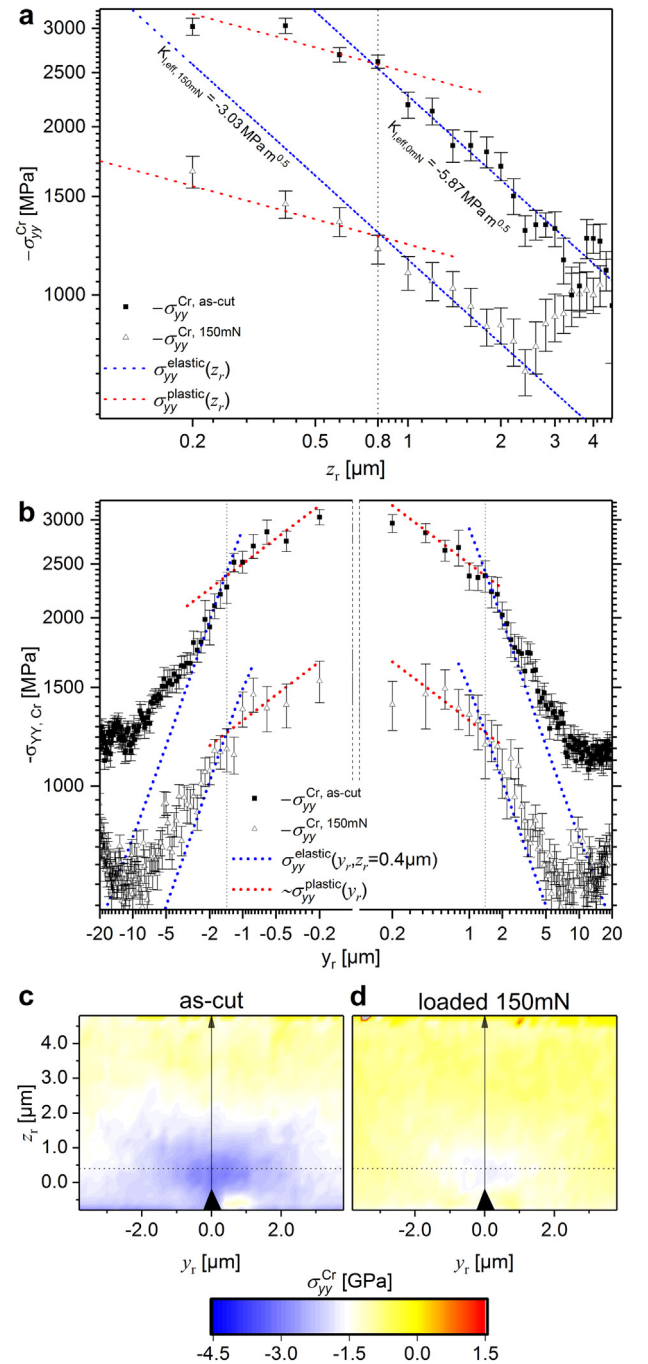


Fig. 7. In-plane/axial stress $\sigma_{yy}^{\text{Cr}}(y, z)$ developed in front of the notch tip in the Cr/HSS sublayer. Experimental data corresponding to the Cr layer at coordinates (a) $z_r = [0.2, 4.6] \mu\text{m}$ (b) and $y_r = [-20, 20] \mu\text{m}$ in the as-fabricated state and at a load of 150 mN. For comparison, power-law-fits for the HRR-dominated plastically deformed zone in front of the notch (red) and the stress-intensity-factor-dominated elastically stressed zone (blue) are also given. The dotted lines at $z_r = 0.8 \mu\text{m}$ and $y_r = \pm 1.5 \mu\text{m}$ in (a) and (b), respectively, indicate the border between elastic and plastic zone. 2D colour plots presented in Fig. 5 are shown here in detail for the area around the notch tip (c) in the as-fabricated state of the cantilever and (d) at a load of 150 mN. The dotted line in (c) and (d) at $z_r = 0.4 \mu\text{m}$ represent the positions, where the data for (b) were obtained.

notch (y outside $\pm 15 \mu\text{m}$, Figs. 5a, 6a) is almost identical to that determined in the film in its as-deposited state (Fig. 3c). Slightly increased compressive stress (add. $\sim 500 \text{ MPa}$) in the upper three layers is mainly related to compressive stress introduced by milling the notch and substrate removal (not quantified here).

According to LEFM, the stress σ_{yy} that develops in front of a crack tip introduced in an ideal linear-elastic material is given by the equation

$$\sigma_{yy} = \frac{K_I}{\sqrt{2\pi r}} \cos \frac{\varphi}{2} \left(1 + \sin \frac{\varphi}{2} \sin \frac{3\varphi}{2} \right) \quad (8)$$

where K_I is the effective stress intensity and r and φ are cylindrical coordinates with the origin located at the crack tip [42]. In the cases of $\varphi = 0$ deg., the equation can be simplified to

$$\sigma_{yy}^{\text{elastic}}(z_r) = \frac{K_I}{\sqrt{2\pi z_r}} \quad (9)$$

and at the centre of the plastic zone,

$$\begin{aligned} \sigma_{yy}^{\text{elastic}}(y_r, z_r = 0.4 \mu\text{m}, \varphi = \arctan \frac{y_r}{0.4 \mu\text{m}}) \\ = \frac{K_I}{\sqrt{2\pi(y_r^2 + (0.4 \mu\text{m})^2)}} \cos \frac{\varphi}{2} \left(1 + \sin \frac{\varphi}{2} \sin \frac{3\varphi}{2} \right) \end{aligned} \quad (10)$$

where z_r and y_r are in a relative orthogonal coordinate system with the same origin as r and φ . σ_{yy} in the directions parallel and perpendicular to the crack is shown in Fig. 7a and b, respectively. Since the residual stress is compressive in all layers, the stress concentration around the notch is also compressive. By applying the experimentally determined stress state to Eqs. 9 and 10, an effective stress intensity of $K_{I, \text{eff}} \sim 5.9 \pm 0.4 \text{ MPa m}^{1/2}$ (cf. Fig. 7a) was calculated [42,43]. Although the change of the stress state brought on by introducing the notch is noticeable in all 4 layers (Fig. 5a), it is most pronounced within a radius of $\sim 4.5\text{--}5 \mu\text{m}$ around the notch, as shown in Fig. 7b. This can be attributed to the presence of the CrN-Cr interface, which possibly hinders the expansion of the elastic field originating at the crack tip.

Within a distance $z_r \leq 800 \text{ nm}$ and $y_r \leq \pm 1.4 \mu\text{m}$ from the crack tip, the stress distributions derived from Eqs. 8, 9 and 10 are no longer corresponding to the experimental data (Fig. 7a, b). This is a consequence of the stress state at the crack tip exceeding the elastic limit of the Cr layer and resulting in the formation of a plastic zone around the crack tip [42]. An in-plane stress of -2.6 GPa was measured at the intersection between elastic and plastic areas, which exceeds the yield stress for nanocrystalline Cr of $\sim 2 \text{ GPa}$ [44,45] and can be related to the significant hydrostatic portion of the stress tensor (cf. Section 3.2.3.4). The data within the plastic zone have thus to be treated considering the crack-tip-singularity and its effect on a power-law hardening of the material as described by Ramberg and Osgood [46], according to the equation derived by Hutchinson [7] and Rice and Rosengren [6] (HRR) for the stress state within the plastic zone originated at the crack tip.

$$\sigma_{rr}(r, \varphi) = C_1(n, \varphi) r^{-\frac{1}{1+n}}, \sigma_{\varphi\varphi}(r, \varphi) = C_2(n, \varphi) r^{-\frac{1}{1+n}} \quad (11)$$

where r and φ are cylindrical coordinates as described above, C is an orientation-dependent variable and n is the power law hardening coefficient ranging from 1 to ∞ , where $n = 1$ and $n = \infty$ represent a linear-elastic material and an elastic-ideal plastic material, respectively [46]. Restricting Eq. 11 to our relative orthogonal coordinate system leads to

$$\sigma_{yy}^{\text{plastic}}(z_r) \equiv \sigma_{\varphi\varphi}(r, \varphi = 0^\circ) = C_2(n, \varphi = 0^\circ) z_r^{-\frac{1}{1+n}}, \text{ and} \quad (12)$$

$$\sigma_{yy}^{\text{plastic}}(y_r) \equiv \sigma_{rr}(r, \varphi) = C_1(n, \varphi = 90^\circ) y_r^{-\frac{1}{1+n}}. \quad (13)$$

The power law hardening coefficient for Cr in front of the crack tip can be roughly estimated from the observed slope $0.15 \approx \frac{1}{1+n}$ in Fig. 7a, b and subsequently yields $n \approx 5.7$, which fits well to literature values for Fe deformed by equal-channel angular pressing, for which $n = \sim 4 - 9$ was determined after considering saturation of the grain size in the nanocrystalline regime [47].

Under elastic loading, the stress state developing inside the cantilever can be described as a sum of stress components originating from (i) the bending of the cantilever beam at a given load, (ii) the stress introduced by the contact with the indenter tip, (iii) the stress developed at the tip of the notch during loading and (iv) the stress associated with the film growth (residual stress), [8,43] and may thus be very high. In order to better understand axial stress changes due to loading, the stress relative to the residual stress in as-fabricated state at $y = -20 \mu\text{m}$ is displayed in Fig. 6c, together with the ideal-elastic loading calculated using the ERM (dashed lines in Fig. 6c, cf. Section 3.3 and Figs. 6b, 10). The experimentally assessed relative axial stress magnitudes at the load of 150 mN in the 4 layers correspond very well to magnitudes theoretically calculated ERM (Fig. 6c). The noticeable deviation between experiment and model in the top CrN layer is highly correlated to the stress introduced by the indenter tip (Fig. 5b) and in agreement to long-range stress profiles measured during indentation [22,23]. The axial compressive stress in this layer reached values of $\sim -4.5 \text{ GPa}$ already at a deflection force of 150 mN (Fig. 6a). The stress field was rather symmetric and the maximum stress was accumulated at an inclination of 30° to the surface normal (Fig. 5b). This stress distribution is determined by the geometry of the indenter tip and the cantilever [22,23]. On the other hand, the stress near the notch tip, exhibiting values of $\sim -2.5 \text{ GPa}$ in the as-fabricated state, was reduced to $\sim -1.6 \text{ GPa}$ at 150 mN load (Fig. 7a, d). According to Eq. 9, this corresponds to an effective stress intensity of $\sim 3.0 \pm 0.5 \text{ MPa m}^{1/2}$. Furthermore, the size of the zone dominated by the elastic field of the crack tip was reduced to $\sim 3 \mu\text{m}$, which is associated with the bending stress counteracting the initial state. Corresponding to the findings above, the size of the plastic zone and the slope of the stresses within did not change after loading to 150 mN , supporting the conclusion that the stress state accumulated through loading to 150 mN (Figs. 5b, 6c and 7) was elastically superimposed onto the initial stress state before bending (Figs. 5a, 6a, c and 7).

The onset of plastic deformation that is detectable by the change of the slope of the load-displacement curve at a load of 450 mN (Fig. 1b) was used to calculate fracture toughness of the lower Cr layer, in which initiation and growth of a crack took place (Fig. 4c). By applying linear-elastic fracture mechanics for the critical load, a value of $2.8 \pm 0.5 \text{ MPa m}^{1/2}$ was obtained, which is in a good agreement with $K_{Ic} \approx 2.5 - 2.7 \text{ MPa m}^{1/2}$ determined by bending of microcantilever beams fabricated from Cr thin films having comparable microstructure and residual stress state [3,45,48].

The axial stress state at a load of 460 mN is shown in Fig. 5c and Fig. 6a. Magnitudes as high as -9 GPa were revealed underneath the indenter tip directly in the contact area (Fig. 5c). Similar values for axial stress have been reported also for other *in situ* and *ex situ* experiments performed on comparable CrN films [23,26]. The stress field in the CrN top-layer underneath the indenter developed at the load of 460 mN (Fig. 5c) is similarly shaped to the stress field observed at 150 mN (Fig. 5b), only the stress values are correspondingly higher. The in-plane stress in the lower Cr interlayer almost fully relaxed due to propagation of the crack through almost the entire Cr layer (Fig. 4c) and induced extensive stress relief in a large volume including also a part of the CrN layer close to the Cr-CrN interface. The relative stress accumulated after loading to 460 mN is shown in Fig. 6c together with the elastic stress profile calculated from ERM. Significant differences from ideal elastic loading are revealed by the experimental data, which can be attributed to (i) a loss of stiffness due to crack growth and stress relaxation in the lower Cr sublayer, (ii) high stress concentrations up to -9 GPa in the top CrN layer as a consequence of indentation and (iii) plastic flow in the top Cr layer as a consequence of compressive stress accumulated through both indentation and bending. Remarkably, directly at the surface of the top CrN layer at $y = \pm 20 \mu\text{m}$, the increase in compressive stress magnitude is in very good agreement with the results from ERM (Fig. 6c), which leads us to conclude that the axial stress

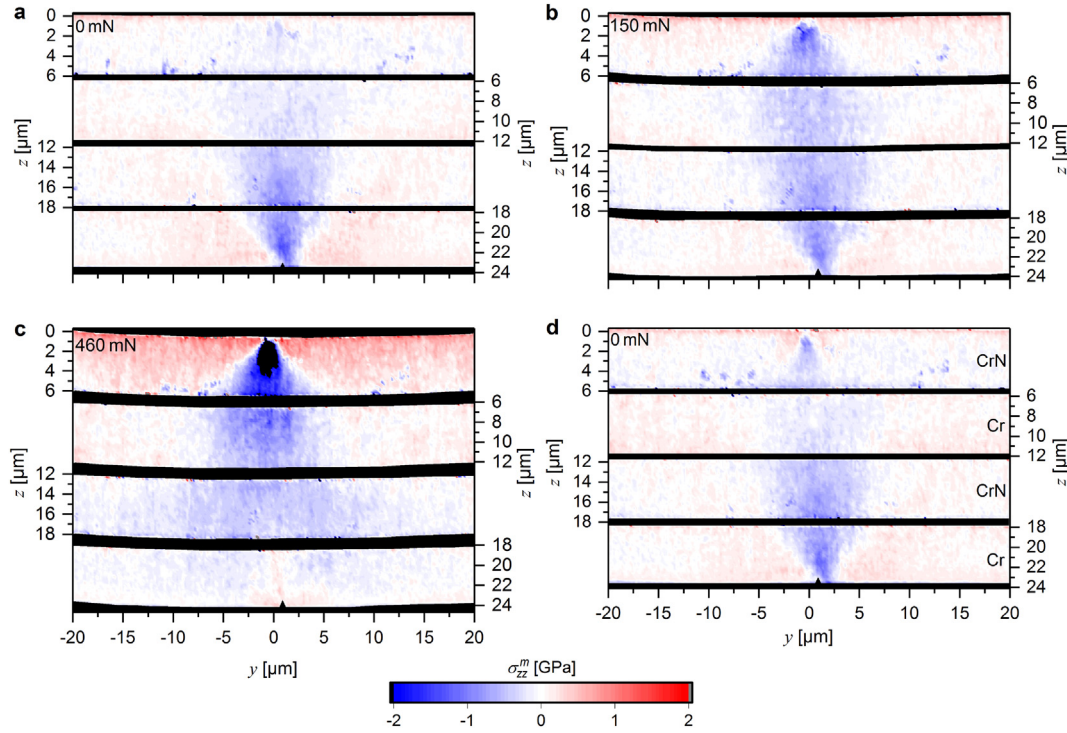


Fig. 8. Out-of-plane/vertical stresses $\sigma_{zz}^m(y,z)$ in the CrN and Cr layers of the clamped cantilever (a) in the as-fabricated state, (b) during loading at 150 mN, (c) at a 460 mN load and (d) after unloading. The data at each individual load step were evaluated from 30,351 2D diffraction patterns.

originated from the indentation are restricted to sub-surface regions [23]. The change of the stress state in both Cr layers from compressive to tensile (~ 700 MPa in the upper and 200 MPa in the lower Cr sublayer) after unloading (Figs. 5d, 6a, c) is associated with the inelastic deformation of the cantilever. For the same reason, the axial stress in the top CrN layer after unloading is more compressive compared to the stress state in its as-fabricated state. Additional compressive residual stress in the centre of the CrN layer is due to plastic deformation near the indenter contact area and also further away in the top Cr sublayer (Fig. 5d). On the contrary, no inelastic stress changes were observed in the lower CrN layer (Fig. 5d), which is due to its position close to the neutral fibre of the clamped cantilever. The compressive stress introduced by milling the notch in the lower Cr layer, which was suppressed during bending of the cantilever, re-emerged after loading and exhibits almost the same value of ~ -2.5 GPa (Fig. 5d). This is related to nearly ideal crack closing and restoration of the material's integrity under compressive load.

3.2.3.2. Experimental out-of-plane stresses. Concerning the out-of-plane stresses $\sigma_{zz}^m(y,z)$ in the as-fabricated state displayed in Fig. 8a, it is evident that the stress distribution is mainly governed by the notch. The out-of-plane stress introduced by a crack tip is given by the equation

$$\sigma_{zz}^{\text{elastic}}(r, \varphi) = \frac{K_I}{\sqrt{2\pi r}} \cos \frac{\varphi}{2} \left(1 - \sin \frac{\varphi}{2} \sin 3 \frac{\varphi}{2} \right) \quad (14)$$

which is only valid as long as $r \ll a$. In the present case, where $r \approx a$, the solution for the crack tip singularity derived by Sneddon [49] has to be used, which takes the non-singular part, i.e. far-field $\sigma_{yy, \infty}$, also into account. This equation can be simplified for the direction parallel to the crack as

$$\sigma_{zz}^{\text{elastic}}(r, \varphi = 0) \equiv \sigma_{zz}^{\text{elastic}}(z_r) = \frac{K_I}{\sqrt{2\pi z_r}} - \sigma_{yy, \infty}. \quad (15)$$

In as-fabricated state, a maximum compressive stress of ~ -1.4 GPa was found at a distance of $\sim 1 \mu\text{m}$ from the crack tip (cf. Fig. 8a, Suppl. Fig. 3a, b). By comparing this value to $\sigma_{yy}(z_r)$ shown in Fig. 7, it can be seen that the stress profiles differ by approximately the amount of in-plane residual stress far off the crack tip, which confirms the applicability of Eq. 15. Comparable deviations of the experimental results from Eq. 14 were found in [13], where the stress in front of the crack in crack opening (y) and crack-growth (z) direction deviated by a factor of ~ 2.5 . Additionally, in contrast to the in-plane/axial stresses, the out-of-plane stress in the cantilever has to fulfil the equilibrium condition at the crack tip, i.e. at free surfaces, stress magnitudes parallel to the surface normal have to be 0, which leads to a reduction of the elastic out-of-plane stress magnitudes within the plastic zone.

As a load of 150 mN is applied to the clamped cantilever, the stress field originated from the notch is reduced as a consequence of the reduced applied stress intensity (Figs. 8b, 7a). Furthermore, the notch-induced stress field is superimposed by the compression field beneath the indenter tip (Fig. 8b), which resulted in two compressive maxima of ~ -0.75 GPa and ~ -1.25 GPa, induced by the notch and impinging indenter tip, respectively. Corresponding to the in-plane stress magnitudes presented in Fig. 8a, the size of the elastic zone in front of the crack tip is reduced to $\sim 3 \mu\text{m}$ (Suppl. Fig. 3a, b). Additionally, at the surface of the topmost CrN sublayer, tensile stress of ~ 0.25 GPa form as a consequence of pile-up formation in the indenter imprint region, which is in agreement with results by Zeilinger *et al.* [22] and Ecker *et al.* [23].

At the maximum load of 460 mN, the stress field induced by the notch mostly disappeared, whereas the out-of-plane compressive indentation-induced stress reached a maximum in excess of -5 GPa (Fig. 8c), which is associated with classical Hertzian contact mechanics [22,23]. At this load, the out-of-plane compressive contact stress penetrated through all layers, and was separated laterally by the stress-free cracked zone in the lowest Cr sublayer as a consequence of crack growth. Furthermore, the tensile stressed zones aside the contact area

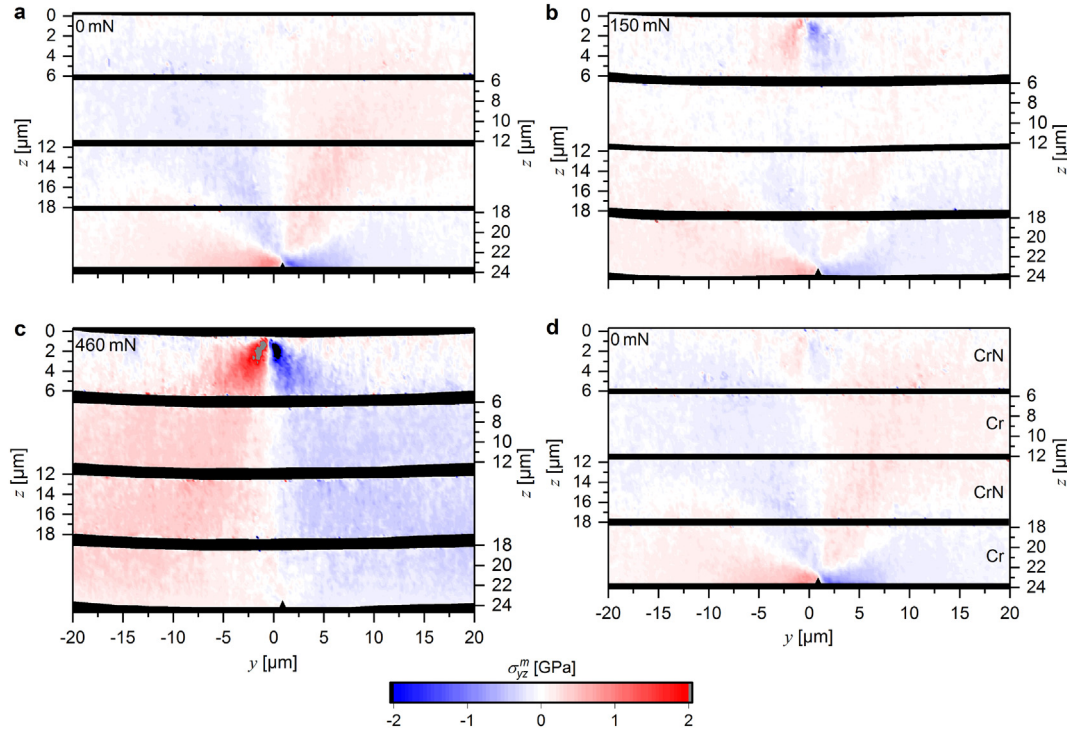


Fig. 9. Shear stresses $\sigma_{yz}^m(y,z)$ in the CrN and Cr layers of the clamped cantilever in (a) the as-fabricated state, (b) during loading at 150 mN, (c) at a 460 mN load and (d) after unloading. The data at each individual load step were evaluated from 30,351 2D diffraction patterns.

with the indenter in the topmost CrN layer reached magnitudes of ~ 1 GPa (Fig. 8c).

After unloading, residual out-of-plane compressive and tensile stress remained around the indentation imprint and additionally, the notch-induced stress field reappeared, which is related to plastic deformation and crack tip blunting in the lower Cr sublayer, as already discussed above (Fig. 8d).

3.2.3.3. Experimental shear stresses. The shear stress $\sigma_{yz}^m(y,z)$ evolution during the in situ experiment is shown in Fig. 9. In the as-fabricated state, notch-induced shear stresses are dominant within all layers (Fig. 9a), reaching a maximum of ± 1 GPa symmetrically next to the notch. Furthermore, the formation of shear stresses appears to be independent of the elastic response of the individual layers and is not interrupted by the interfaces (Fig. 9a). Shear stresses in the crack-tip-area can be described by linear-elastic fracture mechanics as follows

$$\sigma_{yz}^{\text{elastic}}(r, \varphi) = \frac{K_I}{\sqrt{2\pi r}} \cos \frac{\varphi}{2} \sin \frac{\varphi}{2} \cos 3 \frac{\varphi}{2} \quad (16)$$

From Eq. 16 and Fig. 9, it can be seen that the crack-tip shear stresses are 0 along the z_r axis. Perpendicular to the crack tip (along y_r), Eq. 16 can be simplified to

$$|\sigma_{yz}^{\text{elastic}}(y_r)| = \left| \frac{1}{4} \frac{K_I}{\sqrt{\pi |y_r|}} \right| \quad (17)$$

The shear stresses in as-fabricated state perpendicular to the crack tip are shown in Suppl. Fig. 4a and b, from which follows that the observed shear stresses corresponds to an effective stress intensity of $K_{I, \text{eff}} \sim 5.9 \pm 0.4 \text{ MPa m}^{1/2}$, whereas inside the plastic zone, the magnitude decreases.

After loading to 150 mN (Fig. 9b), an indenter-induced shear stress field is introduced in the topmost CrN sublayer according to

Hertzian contact mechanics [22,23]. This shear stress field reaches a magnitude of $\sim \pm 0.5$ GPa symmetrically off-axis beneath the indenter and appears to be restricted to the topmost CrN sublayer, although a superposition of the shear stress induced by the notch and the shear stress induced by the indenter cannot be excluded. Furthermore, the maximum magnitude of the shear field in front of the crack tip is apparently reduced to ± 0.5 GPa, while its extension is restricted to the lower Cr and CrN layers (Fig. 9b). In contrast, the magnitude of the shear fields to the sides of the crack tip is increased, having the same sign as the indenter-induced shear stresses (cf. Suppl. Fig. 4a, c). Additionally, a shear stress τ_{yz} is induced by the bending load acting as a shear force $Q = \mp \frac{P}{2}$, according to

$$\tau_{yz} = \mp \frac{6P}{Bt} \left(\frac{z}{t} - \left(\frac{z}{t} \right)^2 \right) \quad (18)$$

where P is the applied load and t and b are the thickness and width of the cantilever, respectively. Hence, a maximum additional shear stress of ~ 110 MPa was introduced along the neutral fibre axis at a load of 150 mN, whereas this additional shear stress reached ~ 340 MPa at 460 mN. It is obvious that the shear-force induced shear stress counteracted the shear stresses introduced by the notch and the indenter, leading to lower apparent shear stresses in the centre of the clamped cantilever (Fig. 9b, c). This is especially visible at the transition from the lower Cr to the lower CrN sublayer at 150 mN load (Fig. 9b), where the change from positive to negative shear stresses is drawn closer to the symmetry axis, compared to the as-fabricated state (Fig. 9a). After loading to 460 mN, the notch-induced shear stresses disappeared as a consequence of crack growth, whereas the shear stress induced by the indenter tip perpetuated in this case through all layers, reaching maxima of about ± 2 GPa, symmetrically in the topmost CrN sublayer (Fig. 9c). After unloading, again a superposition of indenter tip- and notch-related stress distributions were

observed, indicating inelastic deformation in the topmost CrN sublayer and crack tip blunting in the lowest CrN sublayer, respectively (Fig. 9d).

3.2.3.4. Experimental equivalent von-Mises stresses and experimentally found plastic zone. Equivalent von-Mises stresses were calculated from the experimental data in the area surrounding the notch for plane stress and plane strain state, respectively, using the following equations

$$\sigma_{vM, \text{plane stress}} = \sqrt{\sigma_{yy}^2 + \sigma_{zz}^2 - \sigma_{yy}\sigma_{zz} + 3\sigma_{yz}^2} \quad (19)$$

and

$$\sigma_{vM, \text{plane strain}} = \sqrt{(\sigma_{yy}^2 + \sigma_{zz}^2)(\nu^2 - \nu + 1) + \sigma_{yy}\sigma_{zz}(2\nu^2 - 2\nu - 1) + 3\sigma_{yz}^2} \quad (20)$$

where ν is the Poisson ratio defined for Cr in Table 1. The von-Mises stress state is shown for plane stress and plane strain conditions in Suppl. Figs. 5 and 6, respectively. It can be seen from both Suppl. Figs. that the experimentally determined von-Mises yield stress ranges from 2.0 to 2.3 GPa. Additionally, perpendicular to the crack tip, the plastic zone is apparently elongated to $\sim 3.5 \mu\text{m}$ and is larger compared to that shown in Fig. 7, where the size of the plastic zone was determined to be $1.4 \mu\text{m}$ along the axial (y_r) direction. By replacing σ_{yy} , σ_{zz} and σ_{yz} in Eqs. 18 and 19 with their counterparts from Eqs. 8, 14 and 15 under the assumption of a linear-elastic/ideal plastic material, quadratic equations in $\frac{1}{\sqrt{r_p}}$ were constructed as follows

$$0 = \left(\frac{1}{\sqrt{r_p}}\right)^2 \left(\frac{K_I \cos \frac{\varphi}{2}}{\sqrt{2\pi}}\right)^2 (1 + 3 \sin^2 \frac{\varphi}{2}) + \frac{1}{\sqrt{r_p}} \frac{K_I \cos \frac{\varphi}{2}}{\sqrt{2\pi}} \sigma_{yy, \infty} \left(3 \sin \frac{\varphi}{2} \sin \frac{3\varphi}{2} - 1\right) + \sigma_{yy, \infty}^2 - \sigma_f^2 \quad (21)$$

for plane stress and

$$0 = \left(\frac{1}{\sqrt{r_p}}\right)^2 \left(\frac{K_I \cos \frac{\varphi}{2}}{\sqrt{2\pi}}\right)^2 ((1-2\nu)^2 + 3 \sin^2 \frac{\varphi}{2}) + \frac{1}{\sqrt{r_p}} \frac{K_I \cos \frac{\varphi}{2}}{\sqrt{2\pi}} \sigma_{yy, \infty} \left(3 \sin \frac{\varphi}{2} \sin \frac{3\varphi}{2} - (1-2\nu)^2\right) + \sigma_{yy, \infty}^2 (1 + \nu^2 - \nu) - \sigma_f^2 \quad (22)$$

for plane strain condition, respectively, where $\sigma_{yy, \infty}$ is the stress far off the notch (assumed as constant) and σ_f is the flow stress of Cr. The solutions for plane stress and plane strain conditions are shown in Suppl. Figs. 5c and 6c for values of $\sigma_{yy, \infty} = -1.2 \text{ GPa}$ and $\sigma_f = 2.15 \text{ GPa}$. While the former was obtained from Fig. 3, the latter is a value from literature [44]. The calculated plastic zone in Suppl. Figs. 5c and 6c shows that (i) the size of the plastic zone is less dependent on plane stress and plane strain condition and (ii) that the extension of the plastic zone is significantly larger along the y -axis, contrary to the solutions presented in Ref. [5]. Both results are a consequence of the comparatively higher deviatoric component of the stress tensor in front of the crack tip, caused mostly by the far-field induced reduction of σ_{zz} at distances of $r \approx a$.

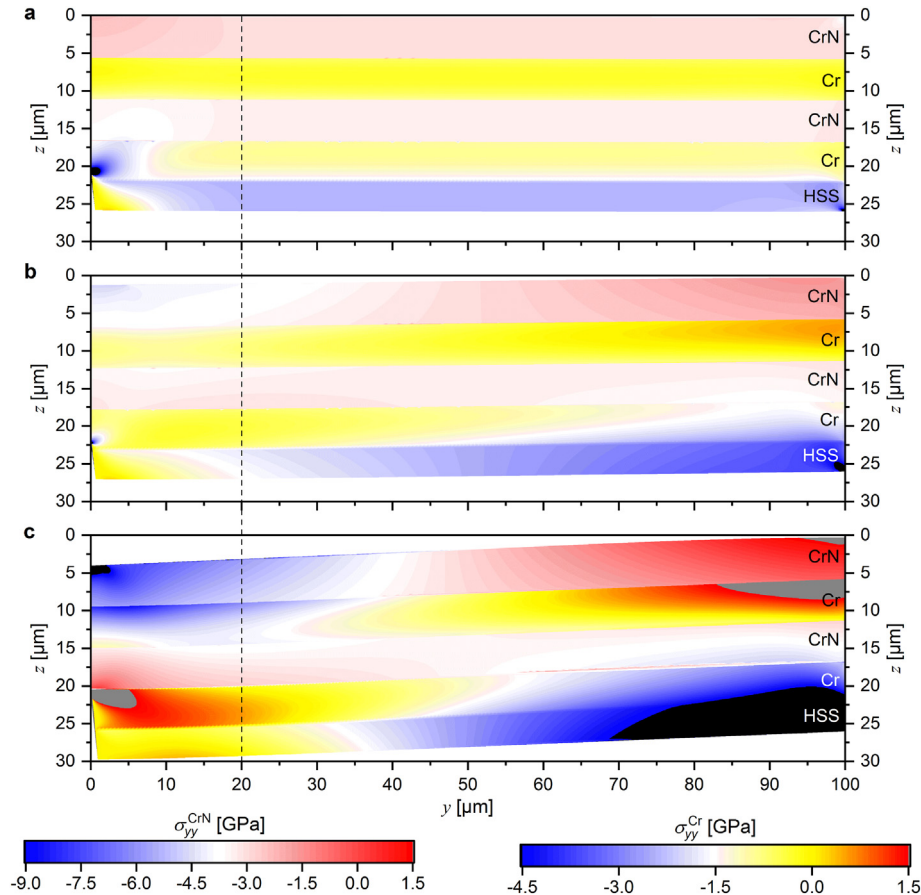


Fig. 10. In-plane/axial stress $\sigma_{yy}^{\text{CrN}}(y, z)$ magnitudes calculated using the ERM for CrN and Cr inside the clamped cantilever in its (a) as-fabricated state, and at loads of (b) 150 mN and (c) 460 mN. The dashed line indicates the edge of the stress fields assessed by the experiment. Note the different stress values in the colour code for CrN and Cr.

3.3. Simulated stress results

After solving the eigenstrain problem using FEM, the in-plane/axial stress $\sigma_{yy}^m(y, z)$ components were obtained (Figs. 6b and 10). A comparison between Figs. 5 and 10 shows excellent agreement between the experimental and simulated experiment for the as-fabricated state ($F_{ind} = 0$ mN, Figs. 5a, 10a) and the first loading step ($F_{ind} = 150$ mN, Figs. 5b, 10b). Before loading, the stress distribution is governed by the residual stress induced by the deposition process and the presence of the notch that acts as a stress raiser both in the experiment (Fig. 5a) and in the model (Fig. 10a). Additional contributions of compressive residual stress were evaluated at the edges of clamping positions, which originate from the boundary conditions, but were not in the measurement area of the experiment. The excellent agreement with experimental data at the edge of the experimentally investigated volume can be seen in Fig. 6, only minor differences were found between experiment (Fig. 6a) and model (Fig. 6b). After applying the first loading step, stress concentrations around corners are reduced and intensified at the top surface and the bottom of the clamped cantilever, respectively (Fig. 10b). Overall, the bending deformation results in additional stress contributions, which are (i) in-plane tensile stress at the clamping positions and compressive in-plane stress in the centre in the top half of the clamped cantilever and (ii) in similar stress distributions of opposite signs formed at the lower half of the clamped cantilever. As a consequence, the stress at the notch tip is significantly reduced, while the stress magnitudes within the experimentally observed regions of the Cr layers still vary between -1.5 GPa and -0.4 GPa and the compressive stress within the CrN layers varies between -4.5 GPa and -2.5 GPa. The calculated stress magnitudes agree particularly well with experimental in-plane stresses $\sigma_{yy}^m(y, z)$ (cf. Fig. 5b, 6a,b and 10), which validates the correct assumption of elastic deformation during loading up to 150 mN. This is furthermore evidenced by Fig. 6c, where the applied stress, i.e. the relative in-plane stress $\Delta\sigma_{yy}^m$ between the individual load steps and the in-plane stress in as-deposited state is shown. There, only minor differences between experiment and model were found for 150 mN applied load.

While the experimentally determined stress distributions (Fig. 5) well agree with the calculated data (Fig. 10) for 150 mN load, they differ for the load of 460 mN. This is likely caused by a combination of two effects: (i) the onset of plastic deformation within both Cr and CrN was not taken into account by the linear-elastic FEM model and (ii) the crack growth through the bottom Cr layer led to a relief and consequent re-distribution of the axial stress component. High stress concentrations around the crack tip, as well as at the penetration point of indenter and at the corner joining the cantilever with the rest of the multilayer become apparent during the final loading step, ranging from 5 GPa tension up to -10 GPa in compression in the model (Fig. 10c). These values probably exceed the elastic limits of nanocrystalline Cr and CrN and it is therefore not surprising to see lower stress values in the experimental data (cf. Figs. 5c, 6 and 10c). In summary, the high accuracy of the FE model confirms the experimental data in the elastic load range and further highlights highly stressed regions at even higher loads, which makes it very easy to identify, by considering the elastic limits of both layer components and the substrate, inelastically deformed and potentially damaged material regions, when comparing simulation and experiment.

4. Discussion

4.1. In situ synchrotron setup and measurement considerations

In previous *ex situ* and *in situ* X-ray diffraction studies, focussed on the determination of stresses in front of a crack tip during fatigue experiments and overload fatigue events, beam sizes (gauge volumes) between 25 and 60 μm have been applied to compact tension samples [11,13–15]. In these studies, normal stresses in the sample volume

and total strain at the surface in front of the crack tip have been investigated using synchrotron X-ray diffraction and DIC, respectively, while the actual crack tip has been tracked at the sample surface using optical microscopy. In only one other study, residual strain and crack closure have been measured *ex situ* after an overload event by a combination of X-ray diffraction and X-ray tomography in the sample volume [10], allowing for separation of plasticity-induced closure and residual stress contributions to fatigue crack retardation following an overload [50]. In contrast, the *in situ* CSnanoXRD setup at the nanofocus beamline (ID13, ESRF) presented in [23] and utilized in this study allowed, for the first time, to determine the stress distributions in the crack-tip area and within the plastic zone with nanoscale resolution for a thin film material (cf. Figs. 5–9). Our work thus represents the first successful attempt to map the full 2D stress tensor perpendicular to the incident X-ray beam including also shear stresses (cf. Figs. 5–9) and simultaneously visualizing the crack and its growth within the investigated volume (cf. Fig. 4). In a first step, validity of the fracture experiment is asserted by the condition

$$a, (t-a), B \geq 2.5 \left(\frac{K_{Ic}}{\sigma_Y} \right)^2 \quad (23)$$

where the cantilever width B , the ligament size $t-a$ and the notch depth a have to be large compared to the process (plastic) zone, which is fulfilled in the present case. Additionally, concerning the formation of a plastic zone in front of the crack tip/notch, the influence of Ga^+ ions from FIB preparation of the sample can be neglected, since the ions penetrate into a depth of only ~ 50 nm below the specimen surface, and influence only an insignificant fraction of the measured plastic zone [51,52]. However, as seen in Eqs. 2 and 3, a drawback of the transmission geometry used in the CSnanoXRD setup is that for low-angle hkl -Debye-Scherrer rings, there is only a very low sensitivity for the normal stress parallel to the beam direction. The stresses retrieved from the experimental diffraction data can, however, be well compared to theoretical considerations of the Griffith model [4] or the HRR stress field [6,7] (cf. Eq. 11). Furthermore, the direct evaluation of K_I using the stresses in front of the crack tip is independent of geometry factors that are otherwise necessary to evaluate the stress intensity and the fracture toughness. The stress distribution perpendicular to the X-ray beam around the crack tip in mode I loading is independent of the presence of plane stress or plane strain conditions, i.e. only the stress component parallel to the beam would differ. On the one hand, the inability to distinguish between these two stress states means that the measurement is exact, but on the other hand, the material properties, especially the plastic behaviour of ductile phases, have to be guessed to a certain degree (cf. Section 3.2.2.4). In the following sections, the effects observed during the *in situ* synchrotron experiment will be discussed with regards to the experimental limitations.

4.2. Stress state around the crack tip in as-fabricated state

Since most studies interested in the residual stress in front of the crack tip have encountered crack propagation during cyclic loading after an overload event [11,13–15], a comparison to our findings can be made especially regarding the stress fields found directly after unloading from an overload event. The overload induces plastic deformation, which relieves (tensile) stresses and in turn generates a compressive residual stress field after unloading. This compressive residual stress field can be assumed to be similar to a residual stress originating from the physical vapour deposition (PVD) process used for the synthesis of thin films. In fact, the σ_{yy} distribution found after unloading from an overload event in Ref. [13] is similar to the one observed in Fig. 5. However, the residual stresses introduced by an overload event are highly localized and non-uniform compared to the laterally uniform residual stresses induced by the PVD process. Secondly, the stress distribution is closely related to the LEFM and EPFM models [5], as shown

in Section 3.2, despite the opposite sign of the stress distributions. Additionally, significant differences between the magnitudes of applied stresses in crack-opening (y) and crack-growth (z) directions were also found in [13,14,53], which is comparable to our findings in Figs. 5a and 8a.

In as-fabricated state, the lower Cr sublayer is compressively stressed up to -1.6 GPa as a consequence of the deposition process. Therefore also the effective stress intensity $K_{I,eff,0mN}$ is negative. Furthermore, the magnitude of the stress intensity due to the residual stresses in as-fabricated state K_{res} ($=K_{I,eff,0mN}$) exceeds the fracture toughness of Cr $K_{IC,Cr} = 2.5\text{--}2.7$ MPa m^{1/2} [3,45] by a factor of 2, which is only possible due to its negative sign. The opposite example can be seen in Ref. [8], where a tensile residual stress present in the material before loading leads to a localized (tensile) stress increase at the crack tip and subsequently significant acceleration of (stable) crack growth.

In our case, a pronounced plastic zone is formed in front of the crack tip, which demonstrates the potential of a crack retardation by compressive residual stress. Consequently, a natural defect, such as droplets, formed within the thin film during processing, would have been enclosed by a plastic zone immediately during thin film growth, due to compressive residual stress as present here for the Cr layer. Furthermore, the evaluation of σ_{yy} in front of the crack tip shows that the approach of LEFM accompanied by small-scale yielding is appropriate, since the stresses at $z_r > 0.8$ μm are characterized by K_I and at smaller distances $z_r = 0.2\text{--}0.8$ μm by the HRR solution [5]. The von-Mises yield stress, presented in Suppl. Figs. 5 and 6 at the intersection between elastic and plastic zone, is in good agreement with the results obtained from micro-pillar compression of ultra-fine grained Cr [44]. Additionally, the shift of the experimentally determined plastic zone in the positive z -direction (compared to the one calculated in Section 3.2.3.4) can be related to the hardening parameter n , as shown in Ref. [5]. In general, the stress state across the clamped cantilever complies very well with theoretical considerations [5–7,49] and experimental results [13], and is also supported, regarding the elastic response, by the 2D FE model (Fig. 10).

4.3. Loading, crack growth, crack tip blunting and crack closing

The comparison of the experimental and calculated results validated that LEFM can be applied to study deformation of the clamped cantilever consisted of Cr and CrN layers. Based on that finding, the applied stress intensity can be added linearly to the effective stress intensity $K_{I,eff,0mN}$, evaluated from the data in as-fabricated state, cf. Ref. [43]. Additionally, according to LEFM, the applied stress intensity is proportional to the applied stress, which is furthermore proportional to the applied indenter load [5]. However, attributing the stresses to their origin during and after loading is rather difficult due to the overlap of (i) crack tip, (ii) indenter, (iii) bending and (iv) residual stress contributions to the overall stress state (cf. Figs. 5–9). In the case of elastic loading, these contributions to the overall measured stress state are accumulated linearly [43], as can be seen when the clamped cantilever is loaded to 150 mN (Fig. 6). During loading to 150 mN, an additional stress intensity K_{app} of 2.9 MPa m^{1/2} thus applied to the crack tip, which resulted in an effective stress intensity of $K_{I,eff,150mN} = -3.0$ MPa m^{1/2}. As already discussed above, the effective stress intensity in front of the crack tip in Cr can be quantified to be negative at 0 and 150 mN load, while the loading can be considered as purely elastic. The reasonability of applying LEFM (and small scale yielding) to analyse fracture behaviour of magnetron sputtered Cr even on a microscale has been validated also in previous studies [3,45].

Unfortunately, no 2D stress pattern was recorded at loads between ~ 300 and 400 mN, which could have resolved the influence of the plastic zone formed in compression on the stresses in tension. However, the influence of the plastic zone formed in front of the crack tip may be minor, since cracks in thin films are supposed to propagate along grain boundaries of low cohesive energy, as seen for example

also in Ref. [48], where intergranular fracture of ultra-fine-grained Cr has been observed during microbending tests. This is furthermore supported by the fact that the fracture toughness calculated from the load-displacement curve and the experimental stress data (under the assumption of LEFM) is comparable to literature values [3,45,48].

When the stress intensity overcomes the fracture toughness of the Cr sublayer, unstable crack starts to grow, which is stopped at the adjacent Cr-CrN interface (Fig. 4c). It results in a loss of geometric stiffness and hence in a rise of applied stresses (while keeping the load constant). Presumably, the applied load then surpasses the elastic limit of the top Cr layer and plastic deformation again reduces the magnitudes of applied stress (Fig. 5c), while the CrN layers still remain loaded elastically (except for the regions surrounding the indenter contact area, Figs. 5c, 8c, 9c).

Additionally, no influence of the crack is visible in the lower CrN layer, indicating that the crack tip has blunted while approaching the still compressively stressed CrN, which is a major difference between the experiment and the linear-elastic 2D FE model (cf. Figs. 5, 10). During further loading, the clamped cantilever would then behave like an unnotched specimen with a discontinuous bottom layer. After unloading, stress fields from the notch reappear (Fig. 5d), uninfluenced by the presence of the crack, which also can be seen in the SAXS micrograph (Fig. 4d). This indicates nearly ideal closing of the crack and restoration of the materials integrity under compressive load.

5. Conclusions

CSnanoXRD was utilized to investigate in situ the nanoscale stress fields in a notched clamped cantilever with a lateral resolution of 200 nm \times 200 nm. The experimentally determined stresses were correlated with small-angle X-ray scattering and electron microscopy and interpreted in light of a 2D elastic finite element model. The compressive stress distribution originating from the deposition process influenced the fracture behaviour significantly, resulting in the immediate formation of a (compressive) plastic zone of considerable size in front of the crack tip in Cr layer. During loading, fracture in the lower Cr layer was retarded by a factor of 3, since the initial (unloaded) stress intensity was double the negative critical value. This demonstrates the beneficial influence of the compressive residual stress and the concept of structural heterogeneity to mechanically stabilize thin films, as demonstrated by the crack stopping ability of heterogeneous interfaces. In summary, it was possible for the first time, to retrieve quantitative information on the nanoscale stress state within the plastic zone during a fracture experiment in nanocrystalline thin films and to manifest the potential of the microstructural design in toughening of hard yet brittle nanostructured materials.

Data availability

Original measurement data are available upon reasonable request.

Declaration of Competing Interest

The authors declare no competing interests.

Acknowledgement

The work has been financially supported by Christian Doppler Research Association. The financial support by the Austrian Federal Ministry of Science, Research and Economy and the National Foundation for Research, Technology and Development is also gratefully acknowledged. Special thanks are devoted to J. F. Keckes for help with the artwork and G. Felber for the mechanical preparation of the synchrotron lamella. Special thanks are also devoted to M. Alfreider for the fruitful discussion about fracture mechanics.

Appendix A. Supplementary data

Supplementary data to this article can be found online at <https://doi.org/10.1016/j.matdes.2020.109365>.

References

- [1] P. Panjan, A. Drnovšek, P. Gselman, M. Čekada, M. Panjan, Review of Growth Defects in Thin Films Prepared by PVD Techniques, 2020 <https://doi.org/10.3390/COATINGS10050447>.
- [2] S. Liu, J.M. Wheeler, J. Michler, X.T. Zeng, W.J. Clegg, Plastic flow at the theoretical yield stress in ceramic films, *Scr. Mater.* 117 (2016) 24–27, <https://doi.org/10.1016/j.scriptamat.2016.02.008>.
- [3] R. Daniel, M. Meindlhummer, J. Zalesak, B. Sartory, A. Zeilinger, C. Mitterer, J. Keckes, Fracture toughness enhancement of brittle nanostructured materials by spatial heterogeneity: a micromechanical proof for CrN/Cr and TiN/SiO_x multilayers, *Mater. Des.* 104 (2016) 227–234, <https://doi.org/10.1016/j.matdes.2016.05.029>.
- [4] A.A. Griffith, The Phenomena of Rupture and Flow in Solids, 1920 163–198, <https://doi.org/10.1098/rspa.1952.0029>.
- [5] T.L. Anderson, *Fracture Mechanics; Fundamentals and Applications*, 4th, CRC Press, Boca Raton, 2017.
- [6] J.R. Rice, G.F. Rosengren, Plane Strain Deformation Near A Crack Tip In A Power Law Hardening Material, 1st16, *Journal of the Mechanics and Physics of Solids*, 1968 1–12, [https://doi.org/10.1016/0022-5096\(68\)900136](https://doi.org/10.1016/0022-5096(68)900136).
- [7] J.W. Hutchinson, Plastic stress and strain at crack tip, *J. Mech. Phys. Solids.* 16 (5) (1968) 337–342, [https://doi.org/10.1016/0022-5096\(68\)900215](https://doi.org/10.1016/0022-5096(68)900215).
- [8] H.E. Coules, G.C.M. Home, K. Abburi Venkata, T. Pirling, The effects of residual stress on elastic-plastic fracture propagation and stability, *Mater. Des.* 143 (2018) 131–140, <https://doi.org/10.1016/j.matdes.2018.01.064>.
- [9] H.E. Coules, G.C.M. Home, Effects of residual stresses and localised strain-hardening on the fracture of ductile materials, *Procedia Struct. Integr.* 17 (2019) 934–941, <https://doi.org/10.1016/j.prostr.2019.08.124>.
- [10] A. Steuwer, L. Edwards, S. Pratihari, S. Ganguly, M. Peel, M.E. Fitzpatrick, T.J. Marrow, P.J. Withers, I. Sinclair, K.D. Singh, N. Gao, T. Buslaps, J.Y. Buffière, In situ analysis of cracks in structural materials using synchrotron X-ray tomography and diffraction, *Nucl. Instrum. Methods Phys. Res. Sect. B Beam Interact. Mater. Atoms.* 246 (2006) 217–225, <https://doi.org/10.1016/j.nimb.2005.12.063>.
- [11] A. Steuwer, M. Rahman, A. Shterenlikht, M.E. Fitzpatrick, L. Edwards, P.J. Withers, The evolution of crack-tip stresses during a fatigue overload event, *Acta Mater.* 58 (2010) 4039–4052, <https://doi.org/10.1016/j.actamat.2010.03.013>.
- [12] P.J. Withers, Fracture mechanics by three-dimensional crack tip synchrotron X-ray microscopy, *Phil. Trans. R. Soc. A* 373 (2015) 0157, <https://doi.org/10.1098/rsta.2013.0157>.
- [13] P. Lopez-Crespo, M. Mostafavi, A. Steuwer, J.F. Kelleher, T. Buslaps, P.J. Withers, Characterisation of overloads in fatigue by 2D strain mapping at the surface and in the bulk, *Fatigue Fract. Eng. Mater. Struct.* 39 (2016) 1040–1048, <https://doi.org/10.1111/ffe.12463>.
- [14] P. Lopez-Crespo, J.V. Peralta, J.F. Kelleher, P.J. Withers, In situ through-thickness analysis of crack tip fields with synchrotron X-ray diffraction, *Int. J. Fatigue* 127 (2019) 500–508, <https://doi.org/10.1016/j.ijfatigue.2019.06.029>.
- [15] W. Zhang, C.A. Simpson, T. Leitner, X. Zhang, R. Pippan, P.J. Withers, The effect of anisotropic microstructure on the crack growth and fatigue overload behaviour of ultrafine-grained nickel, *Acta Mater.* 184 (2020) 225–240, <https://doi.org/10.1016/j.actamat.2019.11.024>.
- [16] J. Ast, M. Ghidelli, K. Durst, M. Göken, M. Sebastiani, A.M. Korsunsky, A review of experimental approaches to fracture toughness evaluation at the micro-scale, *Mater. Des.* 173 (2019) 107762, <https://doi.org/10.1016/j.matdes.2019.107762>.
- [17] M. Alfreider, D. Kozic, O. Kolednik, D. Kiener, In-situ elastic-plastic fracture mechanics on the microscale by means of continuous dynamical testing, *Mater. Des.* 148 (2018) 177–187, <https://doi.org/10.1016/j.matdes.2018.03.051>.
- [18] A.M. Korsunsky, M. Sebastiani, E. Bemporad, Focused ion beam ring drilling for residual stress evaluation, *Mater. Lett.* 63 (2009) 1961–1963, <https://doi.org/10.1016/j.matlet.2009.06.020>.
- [19] M. Sebastiani, E. Rossi, M.Z. Mughal, A. Benedetto, P. Jacquet, E. Salvati, A.M. Korsunsky, Nano-scale residual stress profiling in thin multilayer films with non-equibiaxial stress state, *Nanomaterials* 10 (2020) <https://doi.org/10.3390/nano10050853>.
- [20] E. Salvati, L. Romano-Brandt, M.Z. Mughal, M. Sebastiani, A.M. Korsunsky, Generalised residual stress depth profiling at the nanoscale using focused ion beam milling, *J. Mech. Phys. Solids.* 125 (2019) 488–501, <https://doi.org/10.1016/j.jmps.2019.01.007>.
- [21] A.J.G. Lunt, A.M. Korsunsky, A review of micro-scale focused ion beam milling and digital image correlation analysis for residual stress evaluation and error estimation, *Surf. Coat. Technol.* 283 (2015) 373–388, <https://doi.org/10.1016/j.surfcoat.2015.10.049>.
- [22] A. Zeilinger, J. Todt, C. Krywka, M. Müller, W. Ecker, B. Sartory, M. Meindlhummer, M. Stefanelli, R. Daniel, C. Mitterer, J. Keckes, In-situ observation of cross-sectional microstructural changes and stress distributions in fracturing TiN thin film during Nanoindentation, *Sci. Rep.* 6 (2016) 22670, <https://doi.org/10.1038/srep22670>.
- [23] W. Ecker, J. Keckes, M. Krobath, J. Zalesak, R. Daniel, M. Rosenthal, J. Todt, Nanoscale evolution of stress concentrations and crack morphology in multilayered CrN coating during indentation: experiment and simulation, *Mater. Des.* 188 (2020) 108478, <https://doi.org/10.1016/j.matdes.2020.108478>.
- [24] J. Keckes, R. Daniel, J. Todt, J. Zalesak, B. Sartory, S. Braun, J. Gluch, M. Rosenthal, M. Burghammer, C. Mitterer, S. Niese, A. Kubec, 30 nm X-ray focusing correlates oscillatory stress, texture and structural defect gradients across multilayered TiN-SiO_x thin film, *Acta Mater.* 144 (2018) 862–873, <https://doi.org/10.1016/j.actamat.2017.11.049>.
- [25] J. Keckes, M. Bartosik, R. Daniel, C. Mitterer, G. Maier, W. Ecker, J. Vila-Comamala, C. David, S. Schoeder, M. Burghammer, X-ray nanodiffraction reveals strain and microstructure evolution in nanocrystalline thin films, *Scr. Mater.* 67 (2012) 748–751, <https://doi.org/10.1016/j.scriptamat.2012.07.034>.
- [26] M. Stefanelli, R. Daniel, W. Ecker, D. Kiener, J. Todt, A. Zeilinger, C. Mitterer, M. Burghammer, J. Keckes, X-ray nanodiffraction reveals stress distribution across an indented multilayered CrN-Cr thin film, *Acta Mater.* 85 (2015) 24–31, <https://doi.org/10.1016/j.actamat.2014.11.011>.
- [27] J. Kieffer, D. Karkoulis, J.P. Conf, Related Content PyFAI, A Versatile Library For Azimuthal Regrouping, 2013 8–13, <https://doi.org/10.1088/1742-6596/425/20/202012>.
- [28] G. Ashtotis, A. Deschildre, Z. Nawaz, J.P. Wright, D. Karkoulis, F.E. Picca, J. Kieffer, The fast azimuthal integration Python library: PyFAI, *J. Appl. Crystallogr.* 48 (2015) 510–519, <https://doi.org/10.1107/S1600576715004306>.
- [29] L.A. Feigin, D.I. Svergun, *Structure analysis by small-angle X-ray and neutron scattering*, 1987.
- [30] M. Meindlhummer, N. Jäger, S. Spor, M. Rosenthal, J.F. Keckes, H. Hruby, C. Mitterer, R. Daniel, J. Keckes, J. Todt, Nanoscale residual stress and microstructure gradients across the cutting edge area of a TiN coating on WC co, *Scr. Mater.* 182 (2020) 11–15, <https://doi.org/10.1016/j.scriptamat.2020.02.031>.
- [31] M. Bartosik, R. Daniel, C. Mitterer, I. Matko, M. Burghammer, P.H. Mayrhofer, J. Keckes, Cross-sectional X-ray nanobeam diffraction analysis of a compositionally graded CrN thin film, *Thin Solid Films* 542 (2013) 1–4, <https://doi.org/10.1016/j.tsf.2013.05.102>.
- [32] R. Daniel, K.J. Martinschitz, J. Keckes, C. Mitterer, The origin of stresses in magnetron-sputtered thin films with zone T structures, *Acta Mater.* 58 (2010) 2621–2633, <https://doi.org/10.1016/j.actamat.2009.12.048>.
- [33] J. Almer, U. Lienert, R.L. Peng, C. Schlauer, M. Odén, Strain and texture analysis of coatings using high-energy X-rays, *J. Appl. Phys.* 94 (2003) 697, <https://doi.org/10.1063/1.1582351>.
- [34] J. Pina, A. Dias, M. François, J.L. Lebrun, Residual stresses and crystallographic texture in hard-chromium electroplated coatings, *Surf. Coat. Technol.* 96 (1997) 148–162, [https://doi.org/10.1016/S0257-8972\(97\)00075-3](https://doi.org/10.1016/S0257-8972(97)00075-3).
- [35] A. Riedl, R. Daniel, M. Stefanelli, T. Schöberl, O. Kolednik, C. Mitterer, J. Keckes, A novel approach for determining fracture toughness of hard coatings on the micrometer scale, *Scr. Mater.* 67 (2012) 708–711, <https://doi.org/10.1016/j.scriptamat.2012.06.034>.
- [36] I. Petrov, P.B. Barna, L. Hultman, J.E. Greene, I. Introduction, Microstructural Evolution During Film Growth, 2003 117–128, <https://doi.org/10.1116/1.1601610>.
- [37] R. Daniel, E. Jäger, J. Todt, B. Sartory, C. Mitterer, J. Keckes, Mono-textured nanocrystalline thin films with pronounced stress-gradients: on the role of grain boundaries in the stress evolution, *J. Appl. Phys.* 115 (2014) <https://doi.org/10.1063/1.4879243>.
- [38] R. Daniel, J. Keckes, I. Matko, M. Burghammer, C. Mitterer, Origins of microstructure and stress gradients in nanocrystalline thin films: the role of growth parameters and self-organization, *Acta Mater.* 61 (2013) 6255–6266, <https://doi.org/10.1016/j.actamat.2013.07.009>.
- [39] R. Daniel, D. Holec, M. Bartosik, J. Keckes, C. Mitterer, Size effect of thermal expansion and thermal/intrinsic stresses in nanostructured thin films: experiment and model, *Acta Mater.* 59 (2011) 6631–6645, <https://doi.org/10.1016/j.actamat.2011.07.018>.
- [40] B.N. Jaya, V. Jayaram, Crack Stability in Edge-notched Clamped Beam Specimens: Modeling and Experiments, 2014 213–228, <https://doi.org/10.1007/s10704-014-9956-2>.
- [41] B.N. Jaya, S. Bhowmick, S.A.S. Asif, O.L. Warren, Optimization of clamped beam geometry for fracture toughness testing of micron-scale samples, *Philos. Mag.* 6435 (2015) 1–22, <https://doi.org/10.1080/14786435.2015.1010623>.
- [42] D. Gross, T. Seelig, *Bruchmechanik*, Springer, Berlin, Heidelberg, 2011.
- [43] P.J. Withers, Residual stress and its role in failure, *Rep. Prog. Phys.* 70 (2007) 2211–2264, <https://doi.org/10.1088/0034-4885/70/12/R04>.
- [44] R. Fritz, V. Maier-Kiener, D. Lutz, D. Kiener, Interplay between sample size and grain size: single crystalline vs. ultrafine-grained chromium micropillars, *Mater. Sci. Eng. A* 674 (2016) 626–633, <https://doi.org/10.1016/j.msea.2016.08.015>.
- [45] A. Zeilinger, R. Daniel, M. Stefanelli, B. Sartory, L. Chitu, M. Burghammer, T. Schöberl, O. Kolednik, J. Keckes, C. Mitterer, Mechanical property enhancement in laminates through control of morphology and crystal orientation, *J. Phys. D: Appl. Phys.* 48 (2015) 9, <https://doi.org/10.1088/0022-3727/48/29/295303>.
- [46] W. Ramberg, W.R. Osgood, Description of stress-strain curves by three parameters, *Natl. Adv. Conf. Aeronaut. Technical* 13 (1943).
- [47] J.A. Muñoz Bolaños, O.F. Higuera Cobos, J.M. Cabrera Marrero, Strain hardening behavior of ARMCO iron processed by ECAP, *IOP Conf. Ser. Mater. Sci. Eng.* 2014, p. 63, <https://doi.org/10.1088/1757-899X/63/1/012143>.
- [48] I. Issa, A. Hohenwarter, R. Fritz, D. Kiener, Fracture properties of ultrafine grain chromium correlated to single dislocation processes at room temperature, *J. Mater. Res.* 34 (2019) 2370–2383, <https://doi.org/10.1557/jmr.2019.140>.
- [49] I.N. Sneddon, The distribution of stress in the neighbourhood of a flat elliptical crack in an elastic solid, *Proc. R. Soc. Lond. A* 187 (1946) 229–260, <https://doi.org/10.1098/rspa.1946.0077>.
- [50] E. Salvati, H. Zhang, K.S. Fong, X. Song, A.M. Korsunsky, Separating plasticity-induced closure and residual stress contributions to fatigue crack retardation following an overload, *J. Mech. Phys. Solids.* 98 (2017) 222–235, <https://doi.org/10.1016/j.jmps.2016.10.001>.

- [51] J.P. Best, J. Zechner, I. Shorubalko, J.V. Oboña, J. Wehrs, M. Morstein, J. Michler, A comparison of three different notching ions for small-scale fracture toughness measurement, *Scr. Mater.* 112 (2016) 71–74, <https://doi.org/10.1016/j.scriptamat.2015.09.014>.
- [52] D. Kiener, C. Motz, M. Rester, M. Jenko, G. Dehm, FIB damage of Cu and possible consequences for miniaturized mechanical tests, *Mater. Sci. Eng. A* 459 (2007) 262–272, <https://doi.org/10.1016/j.msea.2007.01.046>.
- [53] P. Lopez-Crespo, P.J. Withers, F. Yusof, H. Dai, A. Steuwer, J.F. Kelleher, T. Buslaps, Overload effects on fatigue crack-tip fields under plane stress conditions: surface and bulk analysis, *Fatigue Fract. Eng. Mater. Struct.* 36 (2013) 75–84, <https://doi.org/10.1111/j.1460-2695.2012.01670.x>.